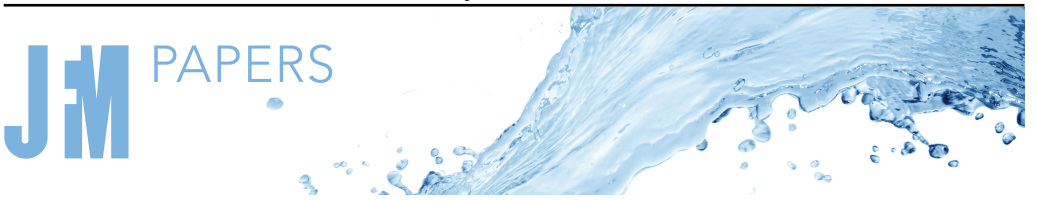
J. Fluid Mech. (2025), *vol.* 1025, A51, doi:10.1017/jfm.2025.10978



Interfacial heat transfer during drop impact on a moving substrate

Reda Kamal[1,2], **Ilia V. Roisman**[1] and **Jeanette Hussong**[1]

[1]Institute for Fluid Mechanics and Aerodynamics, Technische Universität Darmstadt, Peter-Grünberg-Strasse 10, Darmstadt 64289, Germany

[2]Department of Aerospace Science and Technology, Politecnico di Milano, Via La Masa 34, Milano 20156, Italy

Corresponding authors: Reda Kamal, kamal@sla.tu-darmstadt.de; Jeanette Hussong, hussong@sla.tu-darmstadt.de

(Received 4 July 2025; revised 14 October 2025; accepted 7 November 2025)

The thermal interactions of liquid droplets impacting a moving substrate are investigated, combining theoretical modelling with experimental validation. An analytical model is developed to predict the time-evolving contact temperature and heat flux at the droplet–substrate interface. Accounting for the convective heat transport induced by the impacting drop, the model incorporates a finite thermal contact resistance, which is a critical parameter that was often neglected in earlier studies for drop impact. High-speed, spatially resolved infrared thermography is used to record the two-dimensional, transient temperature evolution at the droplet–substrate interface during drop impact on a rotating disc. Measured temperature maps are used for numerical simulations to reconstruct local interfacial heat fluxes. The model is validated for different droplet diameters, substrate velocities and thermal conditions. The findings demonstrate that the substrate velocity and droplet diameter have negligible influence on the thermal behaviour within the tested parameter space.

Key words: drops, aerosols/atomization, breakup/coalescence

1. Introduction

Understanding droplet impact on solid surfaces is critical for various engineering applications, including spray cooling, coating technologies and ice accretion in aeronautical systems. In particular, in icing conditions, droplet impact is the precursor to ice formation, making accurate heat transfer modelling essential for predicting ice growth.

© The Author(s), 2025. Published by Cambridge University Press. This is an Open Access article, distributed under the terms of the Creative Commons Attribution licence (https://creativecommons.org/licenses/by/4.0/), which permits unrestricted re-use, distribution and reproduction, provided the original article is properly cited.

https://doi.org/10.1017/jfm.2025.10978 Published online by Cambridge University Press

This study is motivated by the need to improve thermal modelling in such applications, where droplet impact dictates the initial thermal exchange at the interface. Given its significance in both fundamental research and practical applications, droplet impact has been extensively studied over the years. The interest in this phenomenon dates back nearly one and a half centuries to the pioneering observations of Worthington (1877). As noted by Thoroddsen, Etoh & Takehara (2008), the advent of high-speed imaging techniques has greatly increased interest in this field, providing deeper insights over recent decades. This interest spans multiple fields and applications; for instance, the control and understanding of droplet impact dynamics have led to advancements in spray-based technologies, such as fuel injection in internal combustion engines, as reviewed by Moreira, Moita & Pan (2010). In forensic science, blood-droplet impact patterns have been analysed to reconstruct events, as discussed by Adam (2012), Brodbeck (2012) and Laan *et al.* (2014). Surface engineering has also benefited from research on droplet interactions with complex substrates, as examined by Marengo *et al.* (2011). In icing applications, the thermal exchange initiated by droplet impacts governs the onset of ice buildup on aircraft and power-infrastructure surfaces, as reviewed in Roisman & Tropea (2021). In the aerospace and renewable energy sectors, the ability to control droplet impact is crucial for minimising substrate damage. For instance, Keegan, Nash & Stack (2013) studied the erosion of wind turbines, while Zhang *et al.* (2021) analysed the degradation of protective coatings. These diverse applications highlight the broad relevance of understanding droplet impact across multiple disciplines.

Dimensionless parameters governing the drop impact dynamics and the phenomena associated with drop spreading and splashing include the Reynolds Re and Weber We numbers, which are defined as

$$Re_{d,i} = \frac{\rho_d \mathrm{D} U_{d,i}}{\mu_d}, \quad We_{d,i} = \frac{\rho_d \mathrm{D} U_{d,i}^2}{\sigma_d}, \tag{1.1}$$

where D and $U_{d,i}$ are the drop initial diameter and impact velocity, μ_d, ρ_d and σ_d denote the dynamic viscosity, density and surface tension of the liquid drop, respectively. The subscript i distinguishes whether the parameter is based on the normal, n, or tangential, t, relative velocity component between the droplet and the substrate. The Reynolds number expresses the ratio of inertial to viscous forces in the spreading film, while the Weber number represents the ratio of inertial to capillary forces.

Over the decades, Rein (2002), Yarin (2006), Josserand & Thoroddsen (2016) and Mohammad Karim (2023) have provided comprehensive reviews summarising progress in understanding droplet impact. Early studies primarily focused on cases involving high Reynolds and Weber numbers with single droplets.

For example, Yarin & Weiss (1995) investigated periodic droplet trains impacting substrates and extended theoretical insights to single-droplet impacts on dry surfaces. Their approach introduced a self-similar solution for the internal flow during spreading, which laid the groundwork for subsequent investigations. Building on this foundation, Roisman (2009) and Roisman *et al.* (2009) refined self-similar solutions of the Navier–Stokes equations to predict the maximum spreading diameter and the residual film thickness under isothermal conditions. Subsequently, Riboux & Gordillo (2014) developed theories on the critical impact speed required for drop splashing, which they expanded in Riboux & Gordillo (2015) to quantify the mass and velocities of the ejected droplets. For asymmetric spreading, García-Geijo *et al.* (2020), drawing on the theoretical framework of Gordillo, Riboux & Quintero (2019), predicted the time-evolving shape of the border of the thin liquid film. Xu, Zhang & Nagel (2005) investigated how the surrounding gas pressure affects the stresses and flow fields within the spreading droplet. Additionally, Stow &

https://doi.org/10.1017/jfm.2025.10978 Published online by Cambridge University Press

Hadfield (1981), Range & Feuillebois (1998), Xu (2007), Latka *et al.* (2012), Quetzeri-Santiago, Castrejón-Pita & Castrejón-Pita (2019) and García-Geijo *et al.* (2021) studied the effects of substrate roughness, while Bartolo, Josserand & Bonn (2005), Quéré (2008) and Antonini, Amirfazli & Marengo (2012) emphasised the critical role of wettability. Studies by Antonini, Villa & Marengo (2014), Yeong *et al.* (2014), LeClear *et al.* (2016), Regulagadda, Bakshi & Das (2018) and Aboud & Kietzig (2018) also considered non-axisymmetric impacts and examined the performance of specialised substrates, such as superhydrophobic and icephobic materials, to enhance anti-icing solutions.

Substrate motion introduces an additional complexity, as investigated by Mundo, Sommerfeld & Tropea (1995), Almohammadi & Amirfazli (2017) and Buksh *et al.* (2019). Inclined-impact configurations can replicate certain aspects of a moving substrate at low velocities, as demonstrated by Buksh, Marengo & Amirfazli (2020). However, Povarov *et al.* (1976) and Stumpf *et al.* (2024) reported that sufficiently high substrate speeds generate boundary layers strong enough to induce aerodynamic rebound, resulting in dynamics that do not occur in inclined-impact scenarios.

Although these investigations provided profound insights into isothermal conditions, incorporating thermal effects such as heating, cooling or phase change is still challenging. For example, when the substrate is heated, Senda *et al.* (1988) and Bernardin *et al.* (1997) demonstrated that phenomena like the Leidenfrost effect can significantly alter flow patterns and breakup modes. Understanding these transitions is critical for applications such as spray cooling of hot surfaces, as emphasised by Breitenbach, Roisman & Tropea (2018). Conversely, when a droplet solidifies upon impact, its morphology evolves differently. Such scenarios arise in processes including spray forming, as Orme (1993) described, plasma spray coating, studied by Fauchais (2004), thin-film fabrication, as noted by Steirer *et al.* (2009), and ice accretion in aeronautical applications, as discussed by Cao, Tan & Wu (2018). Accurate characterisation of thermal behaviour at the droplet–substrate interface is essential for predicting and analysing droplet impact outcomes. Tarozzi, Muscio & Tartarini (2007), Teodori *et al.* (2018), Schmidt *et al.* (2020), Gholijani *et al.* (2020) and Gholijani *et al.* (2022) demonstrated that infrared thermography is a highly effective technique for capturing rapidly changing temperature fields during impact. In this study, we utilise an infrared-transparent substrate with an appropriate coating to obtain detailed, two-dimensional (2-D) temperature fields at high temporal resolution, enabling precise measurements of contact temperature distributions and heat fluxes.

Thermal modelling of drop impact has traditionally been based on simplified frameworks since the real problem is rather complicated. For instance, Seki, Kawamura & Sanokawa (1978) proposed for the description of the heat transfer in a droplet suddenly coming into contact with a solid wall to use a one-dimensional (1-D) model for heat conduction in two semi-infinite solid regions (Carslaw & Jaeger 1959). The expressions for the contact temperature T_c and the heat flux at the interface q_c are obtained in the form

$$T_{c,Seki} = \frac{e_d T_d + e_w T_w}{e_d + e_w}, \quad q_{c,Seki} = \frac{e_d e_w (T_w - T_d)}{\sqrt{\pi t}(e_d + e_w)}. \tag{1.2}$$

Here, T_d and T_w represent the temperatures of the liquid and solid, respectively, while e_d and e_w denote their thermal effusivities.

To improve modelling, some studies introduce a finite interfacial resistance R_c to represent the temperature jump and to regularise the early-time $t^{-1/2}$ heat-flux growth (Aziz & Chandra 2000; Chandra & Fauchais 2009). In parallel, to account for the flow inside the drop, Roisman (2009) derived a self-similar spreading-flow solution that Roisman (2010) used to include convective heat transport, although interfacial effects

https://doi.org/10.1017/jfm.2025.10978 Published online by Cambridge University Press

associated with substrate morphology were not considered,

$$T_{c,Roisman} = \frac{e_d T_d + e_w \mathscr{I}(Pr_d, 0, \infty) T_w}{e_d + \mathscr{I}(Pr_d, 0, \infty) e_w}, \quad q_{c,Roisman} = \frac{e_d e_w (T_w - T_d)}{\sqrt{\pi t}(e_d + e_w \mathscr{I}(Pr_d, 0, \infty))}. \tag{1.3}$$

The term $\mathscr{I}$ on the right-hand side of (1.3) accounts for the influence of convective effects in the liquid phase and is a function of the liquid Prandtl number Pr_d, computed in Roisman (2010).

Although several studies have measured contact temperatures on stationary substrates, no corresponding data for moving substrates are available in the existing literature. The validity of the existing models requires an accurate experimental evaluation and validation.

This study has been primarily motivated by the need for improved heat transfer modelling in applications where liquid droplet impact plays a crucial role in ice accretion, setting the stage for subsequent freezing. Specifically, we examine how droplet diameter, substrate speed and thermal boundary conditions influence contact temperatures and heat fluxes. Our theoretical approach builds on the solution obtained in Carslaw & Jaeger (1959), incorporating the convective effect related to the velocity of the spreading drop. These developments are complemented by high-resolution experiments using high-speed imaging and infrared thermography, providing a comprehensive understanding of the flow and thermal fields during the early stages of droplet impact on a moving substrate.

2. Experimental study

2.1. *Experimental set-up*

An experimental set-up was developed to investigate the heat transfer mechanisms during droplet impact. The configuration is schematically illustrated in figure 1. Droplets of double-distilled water are generated within a temperature-controlled cooling chamber (marked 4 in figure 1), ensuring consistent and well-defined initial and ambient conditions. The temperature of the droplets is measured using a type-T thermocouple, marked 5, with an accuracy of $\pm 0.5\,^{\circ}\mathrm{C}$, positioned inside the droplet-generation needle. The cooling system, marked 3, ensures precise control of the droplet's initial temperature. The moving substrate consists of a graphite-coated sapphire disc, marked 8, that serves as the target surface. This substrate is rotated using a geared motor, marked 9, with precise speed control, allowing for accurate setting of the angular velocity. A magnetic encoder, marked 10, is used to provide feedback on the disc's rotation, which is managed by a motor driver controller, marked 11. To synchronise the measurements, a data acquisition system, marked 16, is used, while environmental parameters, such as humidity and temperature, are monitored using a dedicated sensor, marked 13, with data retrieved by a microcontroller, marked 14. The Sensirion SHT85 sensor measures temperature with $\pm 0.1\,^{\circ}\mathrm{C}$ accuracy and relative humidity with $\pm 1.5\,\%$ error. The personal computer, marked 15, is used for data logging and processing. The impact radius, R, is fixed at 73 ± 1 mm, such that no edge effects are present in the boundary layer (Pier 2013). A high-speed camera, marked 2, positioned laterally to the substrate, records the impact dynamics, enabling measurement of the droplet's normal velocity relative to the substrate, $U_{d,n}$, and its diameter, D. The Phantom V2012 high-speed camera operates at 98 900 Hz, with spatial resolution of either 30.9 or 26.7 μm pixel^{-1}, depending on the experiment. A high-speed infrared camera, marked 1, is positioned orthogonally to the substrate's axis of rotation to capture the thermal interactions during droplet impact. The Telops FAST M3k infrared camera covers a spectral range of 1.5–5.4 μm, operates at 2300–8600 Hz, and has a spatial resolution of 73 or 200 μm pixel^{-1}, depending on the experiment.

https://doi.org/10.1017/jfm.2025.10978 Published online by Cambridge University Press

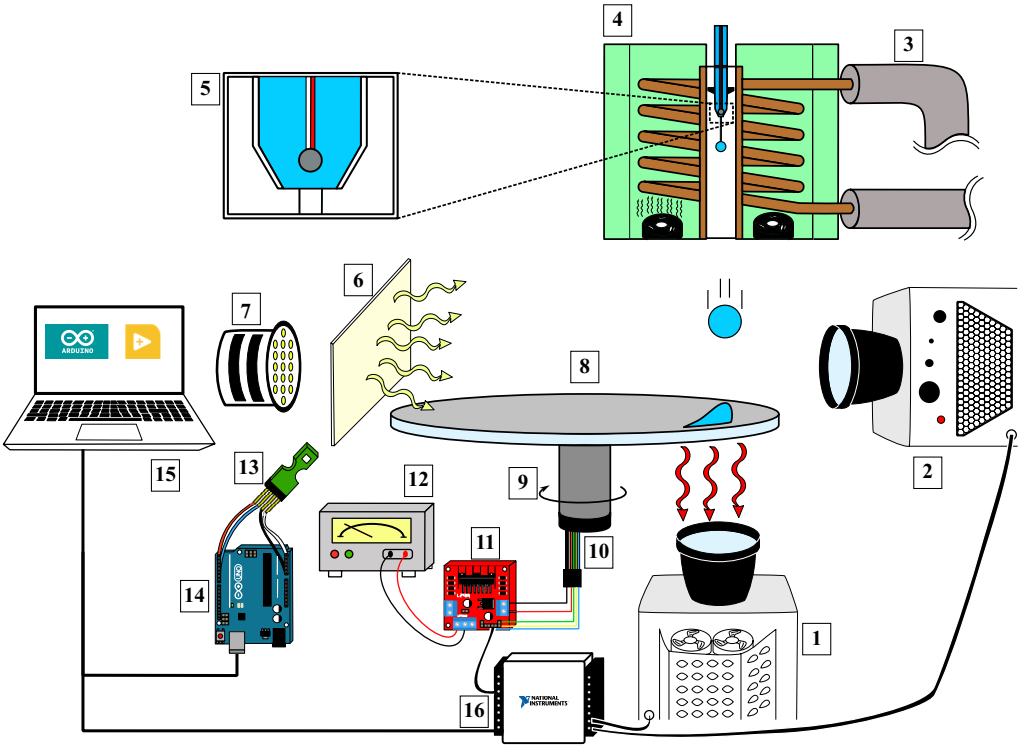


Figure 1. Illustration of the experimental set-up developed to investigate heat transfer during droplet impact. The set-up comprises a droplet-generation system, a rotating sapphire disc as the substrate, high-speed cameras for visualising droplet dynamics, an infrared camera for capturing temperature fields and environmental monitoring equipment.

Exemplary side-view images of the spreading drop are shown in figure 2. These were captured using the high-speed video system, marked 2. Thermocouple measurements are used to extract the corresponding temperature-dependent properties of water from VDI (2013). In the laboratory reference frame, the droplet possesses no tangential velocity. Consequently, its tangential velocity relative to the substrate equals the substrate speed, $\omega R = U_{d,t}$, where ω is the angular velocity of the substrate, derived from the motor's rotational speed, n.

The Reynolds number for the airflow induced by the moving substrate is denoted by $Re_s = \omega R^2/\nu_a$, where ν_a is the kinematic viscosity of air. In these experiments, Re_s ranges from 2000 to 30 000. According to Kobayashi (1994), the critical Reynolds number for the onset of instabilities in the boundary layer, Re_{cr}, is 4.5×10^4. As the maximum Re_s investigated remains below this threshold, the boundary layer surrounding the droplet remains laminar throughout the experimental conditions. Understanding the airflow is crucial, as a strongly turbulent boundary layer, as highlighted by Stumpf *et al.* (2024), can lead to droplet deformation and subsequent aerodynamic rebound. The disc is composed of an infrared-transmissive material (aluminium oxide, α-Al_2O_3, also known as sapphire). To ensure accurate infrared measurements, the impact surface of the disc is coated with a highly emissive graphite-based paint. The influence of this coating on the measurements is considered negligible, an assumption widely supported in the literature (Chaze *et al.* 2019; Gholijani *et al.* 2020; Schmidt *et al.* 2020). The estimated time required for the thermal boundary layer within the coating to develop fully is given by $t \propto \epsilon^2/\alpha_c$, where ϵ

https://doi.org/10.1017/jfm.2025.10978 Published online by Cambridge University Press

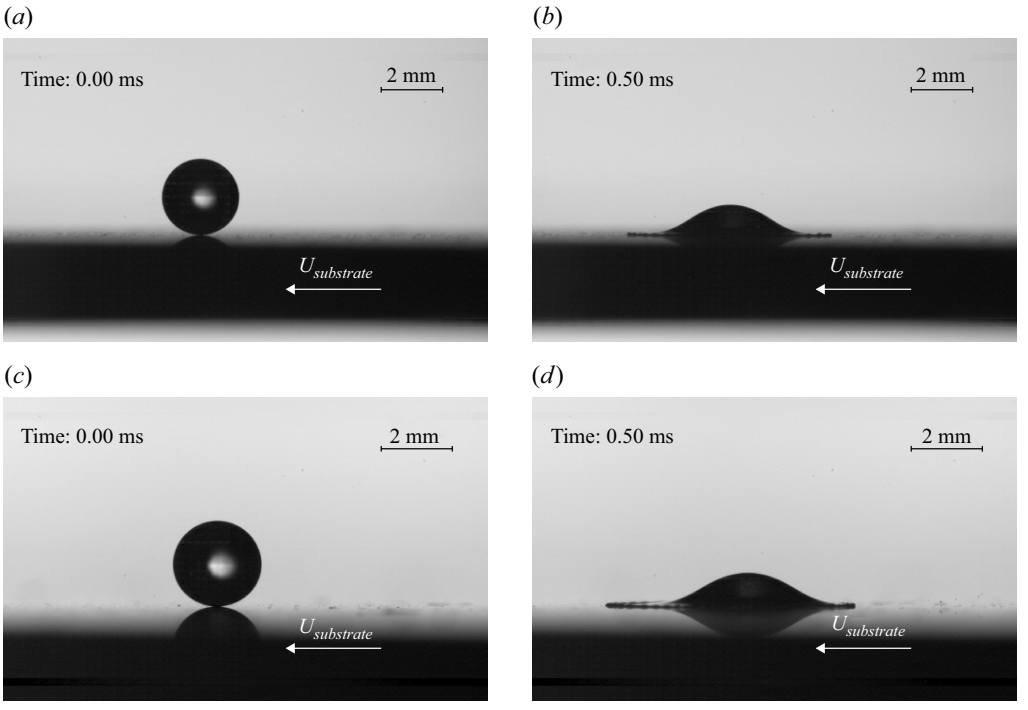


Figure 2. Representative images of droplet impact on a moving substrate. Panels (*a*) and (*b*) show the droplet impact at a substrate velocity of $0.38\,\mathrm{m\,s^{-1}}$, with a droplet diameter $D = 2.45$ mm, normal impact velocity $U_{d,n} = 3.13\,\mathrm{m\,s^{-1}}$, initial droplet temperature $T_{d,0} = 0.5\,^{\circ}\mathrm{C}$ and initial substrate temperature $T_{w,0} = 26.1\,^{\circ}\mathrm{C}$. Panels (*c*) and (*d*) depict the droplet impact at a substrate velocity of $6.12\,\mathrm{m\,s^{-1}}$ under otherwise identical conditions. An asymmetry in the droplet spreading is visible, arising from the increased substrate motion.

denotes the thickness of the coating, and α_c is its thermal diffusivity. In these experiments, the average thickness of the coating is 8 μm, and the thermal diffusivity is approximately $2 \times 10^{-6}\,\mathrm{m^2\,s^{-1}}$. This yields an estimated development time of $t \approx 0.032$ ms, which is significantly shorter than the temporal resolution of $\Delta t = 0.15$ ms given by the infrared camera. The infrared camera is positioned beneath the disc to capture transient temperature measurements during droplet impact. In the experiments, droplet temperature, diameter and substrate speed are systematically varied. The substrate temperature, monitored with temperature sensors, varied with ambient room conditions and ranged from 24.1–33.0 °C across all experiments.

Table 1 summarises the experimental conditions tested in this study. A full factorial design was used to investigate the interactions between these parameters, with the droplet's normal impact velocity held constant.

2.2. *Calibration of the infrared camera*

The infrared camera is calibrated *in situ* using the set-up illustrated in figure 3. A copper plate, cooled by a chiller, extends beyond the camera's entire field of view (FOV), ensuring uniform calibration across the measurement area.

Temperature images are not directly obtained from the infrared camera; instead, the digital level (DL) recorded by the camera is converted into temperature values. The calibration process involves incrementally increasing the temperature of a reference surface from 16–35 °C, with calibration images captured at 1 °C intervals. The variation in DL is recorded as a function of the surface temperature (T), establishing a calibration

https://doi.org/10.1017/jfm.2025.10978 Published online by Cambridge University Press

Parameter	Tested conditions	Maximum uncertainty
D (mm)	1.53, 1.95, 2.45	±0.03
$U_{d,t}$ (m s^{-1})	0.38, 1.53, 3.06, 4.59, 6.11	±0.17
$U_{d,n}$ (m s^{-1})	3.13	±0.15
$T_{d,0}$ (°C)	0.5, 10, 15	±0.5
$Re_{d,n}$	2660−4406	±425
$Re_{d,t}$	1566−13 608	±612
$We_{d,n}$	200−292	±41
$We_{d,t}$	90−1169	±88

Table 1. Summary of the experimental conditions tested in this study. A full factorial design was used to systematically vary droplet diameter (D), substrate speed ($U_{d,t}$) and droplet temperature ($T_{d,0}$). The droplet's normal impact velocity ($U_{d,n}$) was held constant, while key non-dimensional parameters, including the normal and tangential Reynolds ($Re_{d,n}$, $Re_{d,t}$) and Weber numbers ($We_{d,n}$, $We_{d,t}$), were computed over the range of experimental conditions.

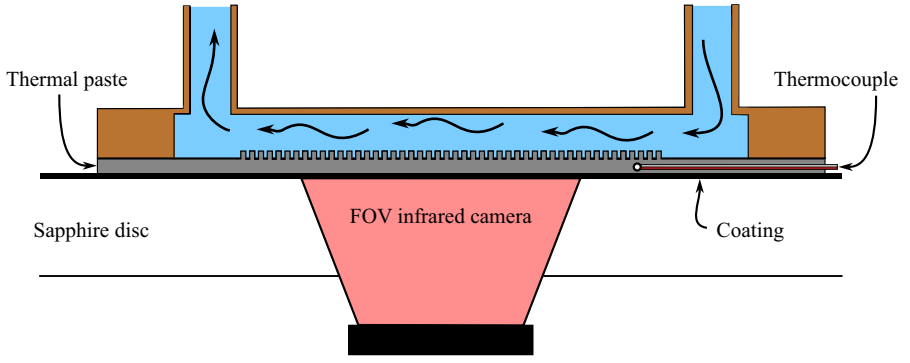


Figure 3. Schematic of the calibration set-up for the infrared camera. The set-up includes a temperature-controlled copper plate thermally coupled to the sapphire disc via a thin layer of thermal paste, ensuring uniform heat transfer. A thermocouple is embedded at the surface to monitor and maintain the substrate temperature accurately. The sapphire disc, coated with a high-emissivity material, serves as the substrate for infrared measurements. The infrared camera captures the temperature distribution at the coating's bottom surface within its FOV.

curve. This relationship between DL and T is governed by Planck's law, which describes the spectral radiant emittance (W_b) of an object as a function of its temperature,

$$W_b(\lambda, T_{obj}) = \frac{2\pi hc^2}{\lambda^5} \frac{1}{\left(e^{\frac{hc}{\lambda k T_{obj}}} - 1\right)}, \tag{2.1}$$

where h is Planck's constant, k is Boltzmann's constant, c is the speed of light, λ is the wavelength and T_{obj} is the temperature of the object.

Numerous studies, including those by Martiny *et al.* (1996), Schulz (2000), Ochs *et al.* (2009), Elfner *et al.* (2017), Falsetti, Sisti & Beard (2021) and Sisti *et al.* (2021), have based their infrared camera calibration on the above equation. By rearranging the terms and isolating T, the following semiempirical relation is obtained:

$$T = \frac{r}{\ln\left(\frac{b}{I_{obj}} + f\right)}, \tag{2.2}$$

https://doi.org/10.1017/jfm.2025.10978 Published online by Cambridge University Press

where I_{obj} is the digital level recorded by the camera, and r, b and f are calibration parameters. These parameters were estimated *in situ* using a thermocouple as the reference and a nonlinear least-squares fitting procedure applied to the calibration images obtained with the set-up illustrated in figure 3.

From the calibration process, two types of errors are quantified: the temporal noise in the temperature readings and the corresponding noise-equivalent heat flux. The temporal noise, σ_T, is defined as

$$\sigma_T = \frac{1}{N_{pixels}} \sum_{j=1}^{N_{pixels}} \sigma_{T,j}, \tag{2.3}$$

where $\sigma_{T,j}$ represents the standard deviation of temperature fluctuations for pixel j across multiple frames i, given by

$$\sigma_{T,j} = \sqrt{\frac{1}{N_{frames}} \sum_{i=1}^{N_{frames}} \left(T_{i,j} - \bar{T}_j\right)^2}. \tag{2.4}$$

Here, N_{pixels} is the total number of pixels in the region of interest, and N_{frames} is the number of frames captured during the calibration measurement. Here $T_{i,j}$ denotes the temperature of pixel j in frame i, and $\bar{T}_j$ is the average temperature of pixel j across all frames. The overall temperature noise, σ_T, is computed as the average of $\sigma_{T,j}$ over all pixels within the region of interest, assuming a spatially uniform temperature distribution.

The calculated temporal noise, σ_T, is 0.21 °C. This value quantifies the variation in temperature readings over time. The corresponding noise-equivalent heat flux is determined separately through numerical simulation of the transient Fourier heat equation applied to the substrate. By analysing the artificial heat flux generated by temperature fluctuations between consecutive frames, the heat flux noise is estimated to be 10^4 W m^{-2}. Further details on the heat flux calculations are provided in § 2.4.

2.3. *Temperature measurements*

The experimental contact temperature values were directly obtained from the infrared camera measurements. A time-lapse sequence of the thermal evolution during droplet impact is shown in figure 4. The colder region represents the area wetted by the droplet, delineated by a sharp temperature gradient in the vicinity of the three-phase contact line. The contact area between the droplet and the substrate increases over time. Figure 4(*a–d*) correspond to four successive time steps: 0.57 ms, 1.03 ms, 1.61 ms and 2.07 ms after impact. As time progresses, the expansion of the contact area results from both droplet spreading and entrainment due to the relative motion with the substrate. To determine a single representative value for the contact temperature, T_c, the average temperature over the droplet–surface contact area was used. This approach is justified by the uniformity of the temperature across the contact region, as evident in figure 4. A slight deviation, specifically a lower temperature difference of approximately 0.2−0.3 °C, is observed in the initial contact area of the droplet, as evidenced in figure 4(*d*). This phenomenon can be attributed to the influence of the droplet's initial normal velocity, which reduces the contact resistance (Aziz & Chandra 2000) and consequently results in a slightly lower contact temperature in this region.

The contact temperature evolutions derived from experiments are given as a function of time for four different substrate velocities in figure 5(*a–d*). In addition to the experimental values and their associated errors, we compare our model with the models of Seki

https://doi.org/10.1017/jfm.2025.10978 Published online by Cambridge University Press

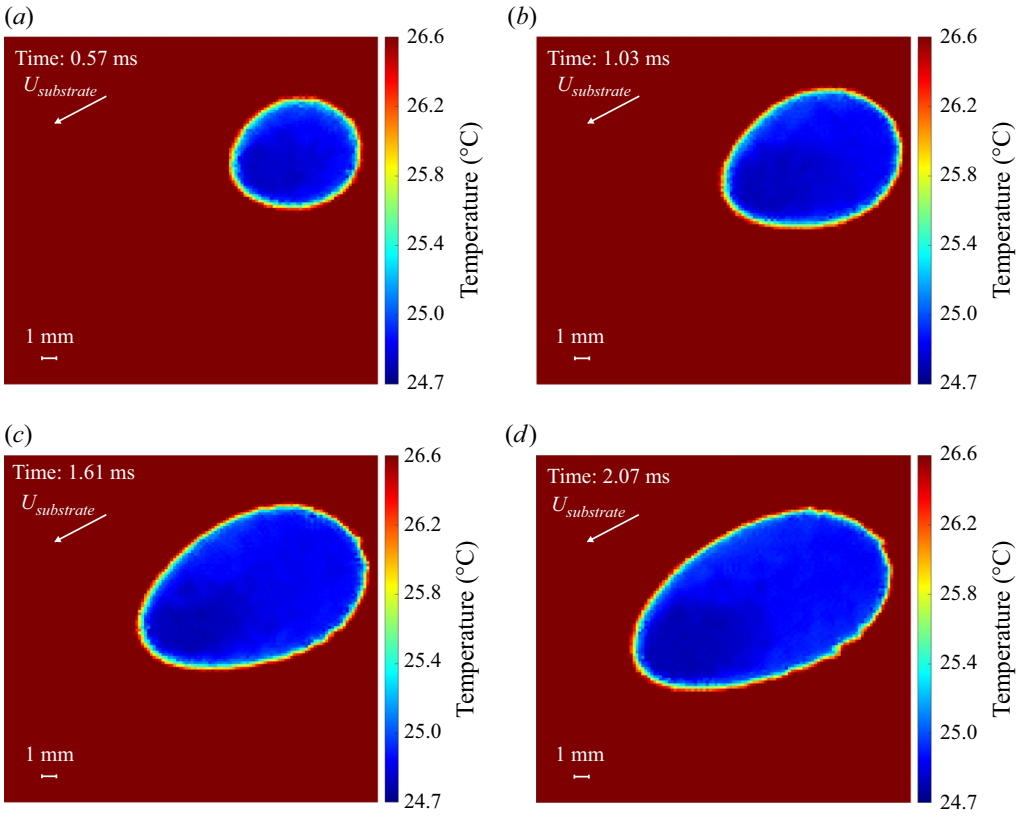


Figure 4. Time-lapse sequence showing the thermal evolution during the impact of a droplet on a moving substrate, recorded using an infrared camera. The droplet, with a diameter of 1.95 mm and an initial temperature of 0.5 °C, impacts a substrate rotating at 800 r.p.m. (6.12 m s^{-1}). Snapshots are taken at different times following impact: 0.57 ms, 1.03 ms, 1.61 ms and 2.07 ms. The temperature distribution within the droplet-substrate contact region remains mostly uniform, with slight deviations observed at the leading edge during initial contact.

et al. (1978) and Roisman (2010), (1.2) and (1.3), respectively. These models predict a constant contact temperature, marked in figure 5 by dashed lines. At the early stages of impact, experimental results show a different behaviour, with the contact temperature decreasing monotonically before reaching the predicted values. We hypothesise that the thermal resistance at the substrate surface causes the temperature evolution. In this study, an improved model has been proposed, which accounts for both convective effects and thermal resistance at the interface. Exemplary results of this model are plotted as blue curves in figure 5(*a–d*). The theoretical framework for the current model is detailed in § 3.

2.4. *Heat flux evaluation*

Heat flux at the wall cannot be directly retrieved from the infrared camera; therefore, a numerical simulation is performed based on the contact temperature measured by the camera. The Fourier heat diffusion equation is solved within the substrate as follows:

$$\frac{\partial T}{\partial t} + \boldsymbol{w} \cdot \boldsymbol{\nabla} T = \alpha_w \nabla^2 T, \tag{2.5}$$

https://doi.org/10.1017/jfm.2025.10978 Published online by Cambridge University Press

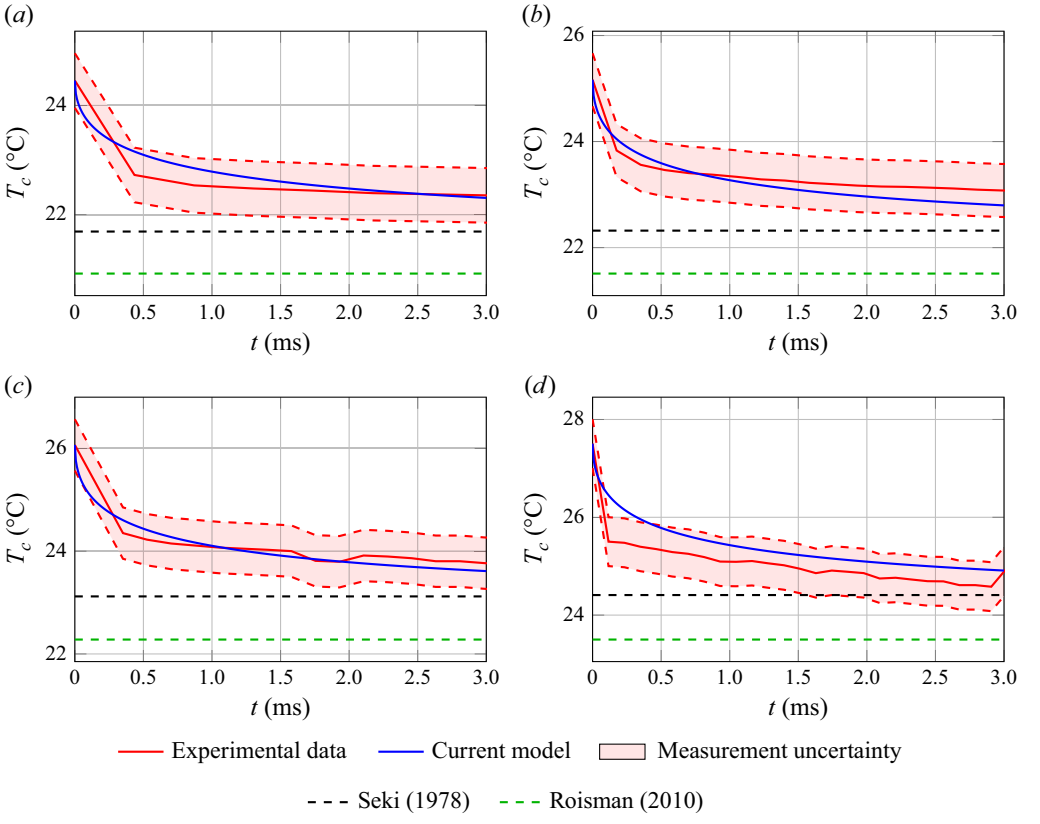


Figure 5. Contact temperature evolution (T_c) over time at different rotational speeds (n). The panels correspond to (*a*) $n = 200$ r.p.m., (*b*) $n = 400$ r.p.m., (*c*) $n = 600$ r.p.m. and (*d*) $n = 800$ r.p.m., for a droplet diameter of $D = 2.45$ mm and an initial droplet temperature of $T_{d,0} = 0.5$ °C. The experimental data (red curve) is compared with the theoretical predictions of the current model (blue curve), with the shaded area indicating the measurement error of the experimental data.

where α_w is the thermal diffusivity of the substrate, and the velocity vector $\boldsymbol{w}$ represents the substrate's motion, as the measurements are taken in the laboratory reference frame. Thermal properties are assumed to remain constant throughout the analysis.

The computational mesh is designed such that the top layer emulates the camera pixels in a one-to-one mapping, with each pixel assigned a velocity vector derived from calibration images acquired during the motion-calibration procedure. The mesh spacing through the substrate thickness and the numerical time step are 3.8 μm and 30.16 μs, respectively. Grid- and time-independence studies are reported in Appendix A. At the interface, a Dirichlet boundary condition is applied, where the temperature is specified using data from the infrared camera. Along the sides of the domain, zero-gradient boundary conditions are imposed. At the bottom, a zero-gradient condition is also applied. This choice is based on the consideration that the substrate is assumed to remain at room temperature, and the heat flux at the bottom is expected to be negligible.

The validity of the assumption is assessed by analysing the effect of the entrained air within the boundary layer, which can lead to heating and a slight increase in temperature. To estimate this effect, the problem is treated analytically by solving a system of ordinary differential equations (ODEs) as described by Millsaps & Pohlhausen (1952), with the

https://doi.org/10.1017/jfm.2025.10978 Published online by Cambridge University Press

boundary condition modified to impose an adiabatic wall instead of a constant temperature. The details of the scaled temperature solution are provided in Appendix B.

Under these conditions, the maximum expected temperature increase for the highest substrate speed is

$$\Delta T_{max} = \frac{(R\omega)^2}{c_{p,a} S(0)} + \frac{\nu_a \omega}{c_{p,a}} Q(0) \approx 0.2\,^{\circ}\mathrm{C}, \tag{2.6}$$

where $S(0)$ and $Q(0)$ are reduced parameters evaluated at the wall based on the ODE solution.

Aside from the theoretical description, this statement is further supported by the experimental findings of Cardone, Astarita & Carlomagno (1994). While the Nusselt number Nu reported in Cardone *et al.* (1994) could, in principle, be used to calculate the heat transfer coefficient h_{tc} for implementing a Robin-type boundary condition, the combination of a very small temperature difference and the uncertainty associated with the coefficient led us to adopt a zero-gradient boundary condition instead. Moreover, it is well established that for elliptic and parabolic equations, boundary effects diminish rapidly with increasing distance from the boundary (Evans 2010).

Finally, preliminary simulations with both bottom boundary conditions (adiabatic and Robin) show that the heat flux at the impact-side interface ($z = 0$) is unchanged. Any differences occur only near the bottom of the substrate, where the magnitude of $\Delta q = q_{Robin} - q_{Neumann}$ is one to two orders of magnitude below the experimental noise, and thus irrelevant for the reconstructed interfacial flux.

3. Heat transfer in a spreading drop, accounting for the thermal contact resistance

3.1. *Problem formulation*

The flow and temperature fields in the spreading droplet must satisfy the continuity, momentum and energy equations (Bird, Stewart & Lightfoot 1966). We assume incompressible flow, as the time scale and spatial region affected by compressibility are negligible in our experiments. This assumption has been thoroughly discussed and validated by Weiss & Yarin (1999). Under these conditions, the governing mass balance, momentum balance and energy balance equations for the Newtonian flow $\boldsymbol{v}$, pressure p and temperature T are written as

$$\boldsymbol{\nabla} \cdot \boldsymbol{v} = 0, \tag{3.1a}$$

$$\rho \frac{\partial \boldsymbol{v}}{\partial t} + \rho(\boldsymbol{v} \cdot \boldsymbol{\nabla})\boldsymbol{v} = -\boldsymbol{\nabla} p + \mu \nabla^2 \boldsymbol{v}, \tag{3.1b}$$

$$\rho c_p \left(\frac{\partial T}{\partial t} + \boldsymbol{v} \cdot \boldsymbol{\nabla} T \right) = k \nabla^2 T. \tag{3.1c}$$

The decoupling of the hydrodynamic problem from the thermal problem is a direct result of assuming constant thermophysical properties. This simplifies the analysis, allowing the temperature field to be solved independently of the velocity and pressure fields. This assumption is appropriate for the regime considered: temperature changes in the liquid remain moderate and are confined to a thin layer near the interface, variations of ρ, c_p and k are much smaller than the change in viscosity, which, in turn influences the thermal problem only indirectly via the advective correction to the similarity velocity $w(z, t)$. A more detailed validation and sensitivity analysis is provided in Appendix C. However, while valid in our parameter range, at larger temperature gradients (leading to

https://doi.org/10.1017/jfm.2025.10978 Published online by Cambridge University Press

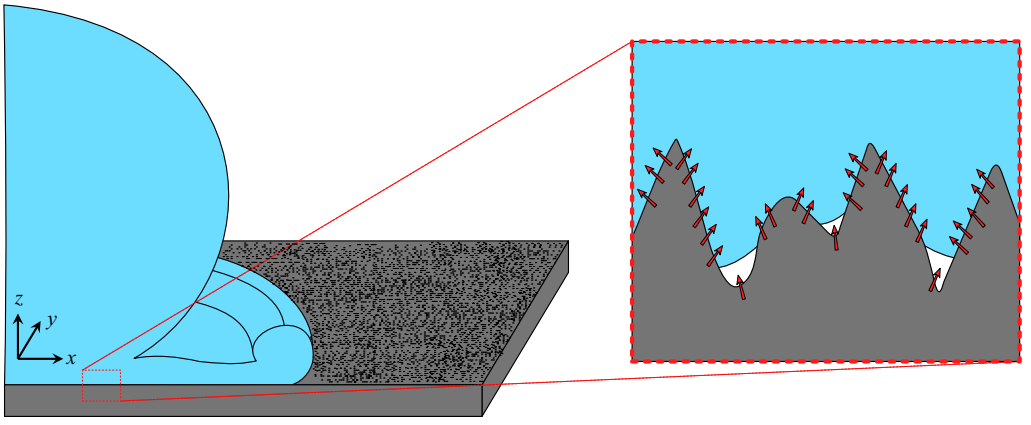


Figure 6. Illustration of droplet impact on a rough substrate, highlighting the interface between the droplet and the substrate. The zoomed-in view emphasises the roughness of the substrate and the liquid–substrate contact area, with the white regions representing entrapped air. The red arrows in the zoomed area represent the heat flux, illustrating local variations where regions with better contact exhibit higher heat flux, while areas with entrapped air show reduced heat flux.

more pronounced property variations), at higher shear rates where viscous heating is non-negligible, or when thermocapillary effects are sufficiently strong to modify the velocity field, a more thorough assessment would be required.

Consider now the Cartesian coordinate system $\{x, y, z\}$ with the unit base vectors $\{\boldsymbol{e}_x, \boldsymbol{e}_y, \boldsymbol{e}_z\}$ with $\boldsymbol{e}_z$ normal to the substrate interface directed towards the drop region. The velocity field in the fluid, which also accounts for the viscous effects, is defined as $\boldsymbol{v} = u\boldsymbol{e}_x + v\boldsymbol{e}_y + w\boldsymbol{e}_z$. The initial conditions and the boundary conditions far from the interface $z = 0$ are expressed as

$$(\boldsymbol{v} - \boldsymbol{v}_0) \times \boldsymbol{e}_z = 0, \quad T = T_{d,0} \quad \text{at } z \to \infty \,\forall\, t > 0 \quad \text{and at } t = 0 \,\forall\, z > 0, \tag{3.2a}$$

$$\boldsymbol{v} = 0, \quad T = T_{w,0} \quad \text{at } z \to -\infty \,\forall\, t > 0 \quad \text{and at } t = 0 \,\forall\, z < 0, \tag{3.2b}$$

where $\boldsymbol{v}_0$ is the velocity in the outer region of the drop far from the viscous boundary layer. The expression for the velocity $\boldsymbol{v}_0$ is obtained as the solution for the inviscid flow in the drop (Yarin & Weiss 1995; Roisman 2010). Here, $T_{d,0}$ and $T_{w,0}$ denote the initial temperatures of the droplet and the substrate, respectively.

The no-slip and zero-flux boundary conditions yield the following boundary conditions for the flow at the interface:

$$\boldsymbol{v} = 0 \quad \text{at} \quad z = 0. \tag{3.3}$$

In this study, the temperature discontinuity arising from the presence of contact resistance between the substrate and the spreading droplet is taken into account. The physical meaning of this thermal resistance is illustrated in figure 6. The thermal effects are influenced by the morphology of the substrate and air entrapment at the interface. The region in the substrate and in the drop, associated with the thermal resistance, is characterised by an effective thickness h_R and effective heat conductivity k_R. In this case the heat flux can be estimated in the form $q \approx k_R(T_d - T_w)/h_R$, where $h_R/k_R \equiv R_c$ is the thermal contact resistance as already proposed by Kapitza (1941), Swartz & Pohl (1989).

The thermal boundary conditions at the interface are expressed as

$$q = k_w \frac{\partial T}{\partial z}\bigg|_{wall} = k_d \frac{\partial T}{\partial z}\bigg|_{drop}, \quad T_d - T_w = q R_c, \quad \text{at} \quad z = 0. \tag{3.4}$$

https://doi.org/10.1017/jfm.2025.10978 Published online by Cambridge University Press

The first equation in (3.4) represents the energy balance at the surface, neglecting the heat accumulated due to the heating of the microscopic contact region, and the second term represents the temperature jump at this contact region.

In this study, we treat R_c as a single, casewise constant effective value, i.e. a lumped, area-averaged interfacial impedance over the inner contact zone. As microroughness and lamella pressure create heterogeneous microcontacts, the interfacial impedance is a function of time and space ($R_c = R_c(x, y, t)$); however, within our 1-D framework, only the area-averaged resistance enters the boundary condition. This simplification is supported by spatially and temporally smooth infrared temperature fields in the central patch of our wetted area (figure 4). We explicitly restrict model–data comparisons with the footprint interior, away from the lamella and rim where a constant R_c assumption would be violated. The same constant R_c closure is common in related droplet-impact and thermal-spray analyses to capture interfacial cooling processes (Dhiman & Chandra 2005; Nastic, Pershin & Mostaghimi 2024). Using this boundary condition, rather than enforcing thermal continuity, reflects the physical reality of many practical systems, where contact resistance cannot be neglected, and highlights a key distinction from prior studies of drop-based cooling that assume perfect thermal continuity at the interface.

3.2. *Viscous flow in the drop region*

The similarity solution for flow within a lamella, expressed in Cartesian coordinates system $\{x, y, z\}$, fixed at the substrate surface, has been obtained in Roisman (2009, 2010),

$$\boldsymbol{v} = f(\xi)\frac{(x + U_x t)\boldsymbol{e}_x + y\boldsymbol{e}_y}{t} - 2\sqrt{\frac{\nu}{t}}g(\xi)\boldsymbol{e}_z, \quad \xi \equiv \frac{z}{\sqrt{\nu t}}. \tag{3.5}$$

Here, $f(\xi)$ and $g(\xi)$ are, respectively, the dimensionless similarity profiles for the tangential and normal velocity components of the boundary-layer flow, where ξ is the similarity variable. At large values of ξ, this field approaches the outer inviscid flow in the spreading drop. The outer solution (Yarin & Weiss 1995; Roisman 2010), which satisfies exactly the mass and momentum balance equations is

$$\boldsymbol{v}_0 = \frac{(x + U_x\tau)\boldsymbol{e}_x + y\boldsymbol{e}_y - 2z\boldsymbol{e}_z}{t}, \tag{3.6}$$

where U_x is the tangential, x-component of the impact velocity relative to the substrate. Here, τ is a time constant; for the present initial condition it takes the value $\tau \approx 0.25\, D_0/U_0$ (see Roisman *et al.* 2009).

Substituting the expression (3.5) in the mass and momentum balance (3.1*a*) and (3.1*b*) yields the following system of ODEs:

$$f = g', \tag{3.7a}$$

$$f'' + \frac{f'}{2}(\xi + 4g) + f = f^2, \tag{3.7b}$$

which can be solved computationally, subject to the no-penetrability conditions and the no-slip conditions at the wall and continuity of the velocity in the outer region

$$f = 1, \quad \text{as } \xi \to \infty, \tag{3.8a}$$

$$g' = g = 0, \quad \text{as } \xi \to 0. \tag{3.8b}$$

For completeness, the functions $g(\xi)$ and $f(\xi)$ first reported in Roisman (2010) are plotted in figure 7.

https://doi.org/10.1017/jfm.2025.10978 Published online by Cambridge University Press

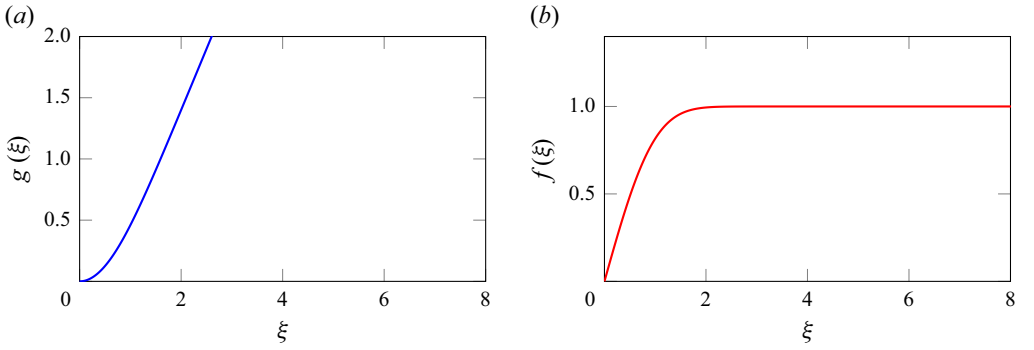


Figure 7. Numerical solutions for the scaled velocity components as functions of the similarity variable ξ. Panel (a) shows the scaled vertical velocity $g(\xi)$, while panel (b) presents the scaled in-plane velocity $f(\xi)$, representing the velocity components in the x–y plane. These results are derived from the coupled ODEs described in (3.7a), (a) The scaled vertical velocity component $g(\xi)$ as a function of ξ. (b)The scaled in-plane velocity component $f(\xi)$ (in the x–y plane) as a function of ξ.

3.3. *Heat transfer in the drop and substrate at high Prandtl numbers $Pr_d \gg 1$*

Assuming contact resistance, the temperature fields in the spreading drop $z \geqslant 0$ and the solid substrate $z \leqslant 0$ are represented using the known analytical solution for heat conduction. For the solid region, the solution that exactly satisfies the energy equation together with the boundary and initial conditions is given in Carslaw & Jaeger (1959) as

$$T_w = T_{c0} + (T_{w0} - T_{c0}) \left[\exp\left(\frac{t}{t_R} - 2\zeta_w \sqrt{\frac{t}{t_R}} \right) \operatorname{erfc}\left(\sqrt{\frac{t}{t_R}} - \zeta_w \right) - \operatorname{erf}(\zeta_w) \right], \quad (3.9a)$$

$$\zeta_w \equiv \frac{z}{2\sqrt{\alpha_w t}}, \quad (3.9b)$$

where T_{c0} is a constant temperature equal to the asymptotic value of the contact temperature at long times, and t_R is a characteristic time associated with the duration of the propagation of the thermal boundary layer inside the contact region of thickness h_R. These constants will be determined from the boundary conditions. Here ζ_w is the similarity variable in the solid region. The energy equation in the liquid region has to account for the heat convection. Therefore, in contrast to the purely diffusive semi-infinite solution used for the solid (Carslaw & Jaeger 1959), we adopt a similarity ansatz that extends that diffusion form to include advection. We thus write for the spreading drop

$$T_d = T_{c0} + (T_{d0} - T_{c0}) \left[c_d \exp\left(\frac{t}{t_R} + 2\zeta_d \sqrt{\frac{t}{t_R}} \right) \operatorname{erfc}\left(\sqrt{\frac{t}{t_R}} + \zeta_d \right) + \theta(\zeta_d) \right], \quad (3.9c)$$

$$\zeta_d \equiv \frac{z}{2\sqrt{\alpha_d t}}, \quad (3.9d)$$

where α_d is the thermal diffusivity of the drop, c_d is a constant and the function $\theta(\zeta_d)$ is the self-similar component of the temperature field associated with convective transport in the drop. Here ζ_d is the similarity variable in the liquid region. In essence, the exponential factor in (3.9a) encodes the effects of finite contact resistance, and the classical $\operatorname{erf}(\zeta)$ term describes the response of a semi-infinite conductor under pure thermal diffusion. In the droplet, this term is replaced by the self-similar convective kernel θ to account for thermal

https://doi.org/10.1017/jfm.2025.10978 Published online by Cambridge University Press

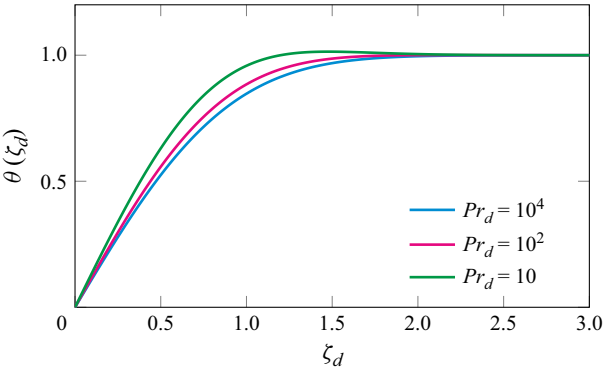


Figure 8. Theoretically predicted values of $\theta(\zeta_d)$ at various values of the Prandtl number.

diffusion and advection in the flow. The kernel θ is obtained from early-time asymptotics of the coupled advection–diffusion problem, as described later.

Expression (3.9*a*) satisfies the heat conduction equation in the wall exactly. However, the form (3.9*c*) yields only an approximate solution for the temperature field in the drop if the convective terms are smaller than the conductive terms. In the case of a large Prandtl number,

$$Pr_d \equiv \sqrt{\frac{\nu_d}{\alpha_d}}, \tag{3.10}$$

the thickness of the thermal boundary layer is much smaller than that of the viscous boundary layer. In this case, since both the value of the normal velocity and its gradient at the wall are equal to zero, the convection effects are indeed small. The validity of this assumption is assessed in Appendix D, where we compare the closed-form model with an independent advection–diffusion numerical reference. The asymptotic expression for the gradient of the drop temperature taking into account a small value of t_R/t is obtained from (3.9*c*) in the form

$$\frac{\partial T_d}{\partial z} \approx \frac{(T_{d0} - T_{c0})}{2\sqrt{\alpha_d t}} \left[\exp\left(-\zeta_d^2\right)\theta'(0) + \theta'(\zeta)\right], \quad \text{if} \quad t \gg t_R. \tag{3.11}$$

This approximate expression can be used for the estimation of the small convective terms in the energy equation if the Prandtl number is large.

Substitution of expressions (3.9) and (3.11) in the energy (3.1*c*) yields the following similarity equation:

$$\theta''(\zeta_d) + 2\zeta_d\theta'(\zeta_d) + 4Pr_d^{1/2} g\left[\frac{\zeta_d}{Pr_d^{1/2}}\right]\left\{\theta'(\zeta_d) + \exp\left(-\zeta_d^2\right)\theta'(0)\right\} = 0, \tag{3.12}$$

where the dimensionless function g is determined from the similarity solution for the drop velocity field.

This ODE has to be solved subject to the boundary conditions

$$\theta = 0, \quad \text{at} \quad \zeta_d = 0, \tag{3.13a}$$

$$\theta \to 1, \quad \text{as} \quad \zeta_d \to \infty. \tag{3.13b}$$

In figure 8, the theoretical predictions for the dimensionless function $\theta(\zeta_d)$ are shown for various Prandtl numbers. The computed values of $\theta'(0)$ as a function of Pr_d are shown in figure 9. The value of the constants T_{c0} and t_R are determined from the boundary

https://doi.org/10.1017/jfm.2025.10978 Published online by Cambridge University Press

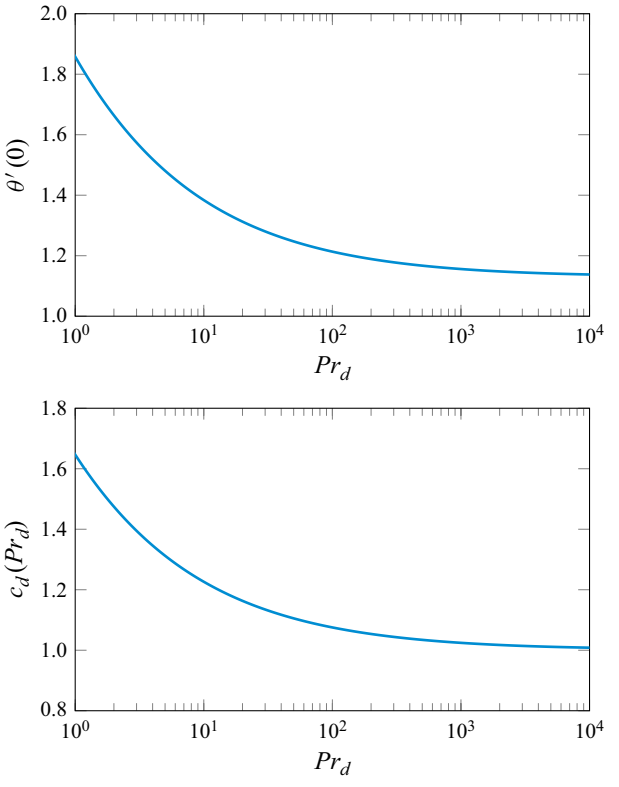


Figure 9. Theoretically predicted values of $\theta'(0)$ and c_d as a function of the Prandtl number.

conditions (3.4) associated with the thermal contact resistance

$$T_{c0} = \frac{e_w T_{w0} + e_d c_d T_{d0}}{e_w + e_d c_d}, \quad t_R = \left(\frac{e_d e_w}{e_d + e_w} R_c\right)^2, \quad c_d = \frac{\sqrt{\pi}\theta'(0)}{2}, \tag{3.14}$$

where $\theta(\zeta_d)$ is a dimensionless function given in (3.9*c*), e_d and e_w are the thermal effusivities of the drop and substrate materials, respectively. Finally, the substrate temperature at the interface $z = 0$ and the heat flux are obtained using (3.9) in the form

$$T_{w,interface} = T_{c0} + (T_{w0} - T_{c0})\exp\left(\frac{t}{t_R}\right)\operatorname{erfc}\left(\sqrt{\frac{t}{t_R}}\right), \tag{3.15a}$$

$$q_{interface} = \frac{T_{d0} - T_{w0}}{\sqrt{t_R}} \frac{e_w\, e_d\, \sqrt{\pi}\, \theta'(0)}{2\, e_w + e_d\, \sqrt{\pi}\, \theta'(0)} \exp\left(\frac{t}{t_R}\right)\operatorname{erfc}\left(\sqrt{\frac{t}{t_R}}\right). \tag{3.15b}$$

Equations (3.15*a*) and (3.15*b*) incorporate the influence of substrate morphology, resulting in a time-dependent interfacial temperature. Unlike (1.2) and (1.3), they preserve both the conductive mechanisms of Seki *et al.* (1978) and the convective effects described by Roisman (2010). The value of the thermal contact resistance, R_c, required to determine the characteristic time scale t_R was obtained by fitting the analytical substrate–temperature evolution (3.15*a*) to each experimental curve and subsequently averaging the results. The mean value was found to be 2.39×10^{-5} m^{2}K W^{-1} with a 95 % confidence interval of $[1.73 \times 10^{-5}, 3.65 \times 10^{-5}]$ m^{2}K W^{-1}.

A comparison between the experimental results and the three models can be seen in figure 10(*a–c*). For the models of Seki *et al.* (1978) and Roisman (2010), which predict a

https://doi.org/10.1017/jfm.2025.10978 Published online by Cambridge University Press

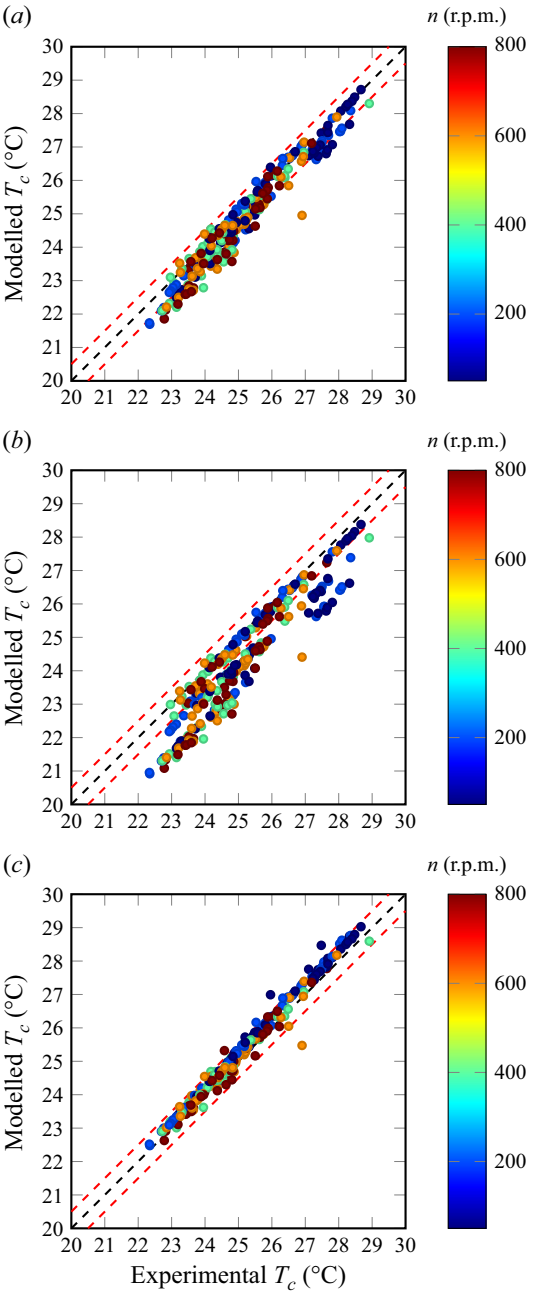


Figure 10. Comparison of experimental contact temperatures with theoretical predictions for various models: (*a*) Seki *et al.* (1978); (*b*) Roisman (2010); (*c*) the current model. Each plot includes experimental data (circles), a line of perfect agreement (black dashed) and experimental error bounds (red dashed).

time-independent interfacial temperature, we perform the comparison at the instant when the measured interfacial temperature attains its local minimum. The model of Seki *et al.* (1978) has a rather fair agreement as shown in figure 10(*a*), which can be explained by the fact that for our investigated Pr_d, the convective effects are small and the underestimation of the contact temperature is balanced by the missing contact resistance condition. On

https://doi.org/10.1017/jfm.2025.10978 Published online by Cambridge University Press

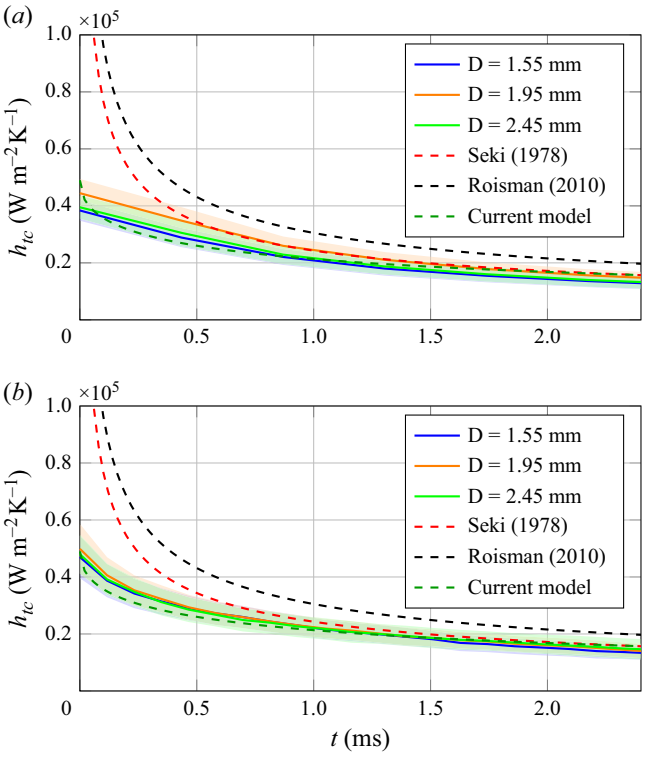


Figure 11. Heat transfer coefficient, h_{tc}, as a function of time, t, for different rotational speeds and droplet diameters. Experimental data (solid lines) are compared with theoretical predictions (dashed lines). Panels (a) and (b) correspond to substrate rotational speeds of 200 and 800 r.p.m., respectively. Shaded regions indicate measurement uncertainty.

the other hand, the model of Roisman (2010) consistently underestimates the contact temperature due to the missing contact resistance term. The present model incorporates both heat convection and contact resistance, resulting in a very good agreement with the experimental data.

The heat transfer coefficient at the interface is readily derived by scaling the heat flux to the initial temperature difference between the substrate and the spreading drop as

$$h_{tc} = \frac{q}{\Delta T} = \frac{e_w e_d \sqrt{\pi}\theta'(0)}{\sqrt{t_R}(2e_w + e_d\sqrt{\pi}\theta'(0))} \exp\left(\frac{t}{t_R}\right) \operatorname{erfc}\left(\sqrt{\frac{t}{t_R}}\right), \tag{3.16}$$

where $\Delta T = T_{d0} - T_{w0}$ is the initial temperature difference between the droplet and the substrate. This quantity is plotted in figures 11(a) and 11(b) for the two extreme substrate velocities tested (≈200 and 800 r.p.m.), each at varying droplet diameters. Intermediate velocities were also investigated and exhibited qualitatively similar trends; they are therefore omitted here for conciseness. As expected, neither the droplet diameter nor the substrate velocity significantly affects the heat flux. This is consistent with the theoretical model predictions. The results demonstrate good agreement between experimental data (solid lines) and theoretical predictions (dashed lines), as shown in figure 11, where shaded regions represent measurement uncertainty. The present model applies to early-time, conduction-dominated exchange with finite interfacial resistance and no phase change. Two practical bounds are worth noting: at very high substrate speeds, large shear rates

https://doi.org/10.1017/jfm.2025.10978 Published online by Cambridge University Press

can introduce viscous heating and strong advection, which are not included here; and for very small (micronscale) droplets, the semi-infinite-liquid and locally 1-D assumptions may fail and free-surface effects may become important. Conversely, for larger droplets, the assumptions remain valid. Furthermore, regimes involving phase change (boiling, evaporation, solidification) are outside the scope of this study. For completeness, we propagate the estimated uncertainty in the interfacial resistance R_c into the predicted heat-transfer coefficient $h_{tc}(t)$; the procedure and the resulting 95 % confidence intervals are given in Appendix E. These intervals are consistent with the experimental ones. While the contact–temperature points in figure 10 differ only modestly through the models, the corresponding heat flux, and therefore $h_{tc}(t)$, shows larger differences between the models. This arises from including the contact–resistance boundary condition, which yields a finite heat flux at $t = 0$, in contrast to the initial singularity predicted by the models of Seki *et al.* (1978) and Roisman (2010). This finite behaviour highlights the importance of incorporating realistic boundary conditions in heat transfer models to accurately capture interfacial dynamics during droplet impact.

4. Conclusion

This study presents a comprehensive theoretical and experimental investigation of the thermal interactions during the impact of liquid droplets on a moving solid substrate. We develop a closed-form model that simultaneously accounts for conduction in the wall, convective heat transport within the spreading droplet and substrate-morphology effects via a finite interfacial contact resistance R_c. By extending the self-similar spreading solution of Roisman (2010), the revised framework yields closed-form expressions for both interfacial temperature and heat flux that remain finite and physically realistic throughout the impact process. The model is validated through high-speed, spatially resolved infrared thermography, which captures the 2-D, transient temperature evolution at the droplet–substrate interface during impingement on a rotating, infrared-transmissive sapphire disc coated with a highly emissive graphite-based layer. The experimental temperature maps are used to numerically reconstruct local interfacial heat fluxes, which show strong agreement with the theoretical predictions. Across a range of droplet diameters, substrate velocities, and thermal conditions – including normal and tangential Reynolds numbers ($Re_{d,n} \approx 2660-4406$, $Re_{d,t} \approx 1566-13\,608$) and Weber numbers ($We_{d,n} \approx 200-292$, $We_{d,t} \approx 90-1169$), the thermal behaviour is found to be insensitive to variations in droplet size and substrate speed. This confirms the robustness of the model and supports the theoretical prediction that these parameters have a negligible influence on interfacial heat transfer under the studied conditions.

Supplementary movies. Supplementary movies are available at https://doi.org/10.1017/jfm.2025.10978.

Acknowledgements. The authors gratefully acknowledge Dr-Ing. M. Lausch for his invaluable insights and stimulating discussions throughout this work, which greatly enhanced its quality and rigour. We also thank O.U.R. Siddiqui for his assistance with the experimental programme. Parts of this work have been improved grammatically and stylistically using language models, including Chat-GPT (OpenAI) and DeepL Write (DeepL SE).

Funding. The work of R.K. was funded by the European Union's Horizon Europe research and innovation programme under the Marie Skłodowska-Curie grant agreement no. 101072551 (TRACES). The work of J.H. and I.V.R. is partially supported by the joint DFG/FWF Collaborative Research Centre CREATOR (DFG: Project-ID 492661287/TRR 361; FWF: 10.55776/F90) at TU Darmstadt, TU Graz and JKU Linz.

Declaration of interests. The authors report no conflict of interest.

https://doi.org/10.1017/jfm.2025.10978 Published online by Cambridge University Press

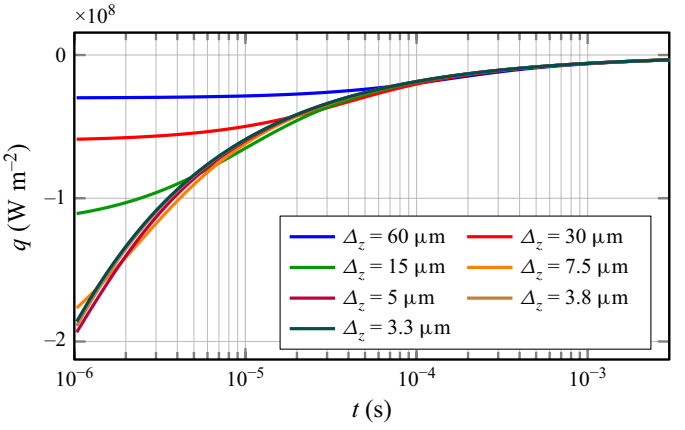


Figure 12. Surface heat flux $q(t)$ for several through-thickness grids.

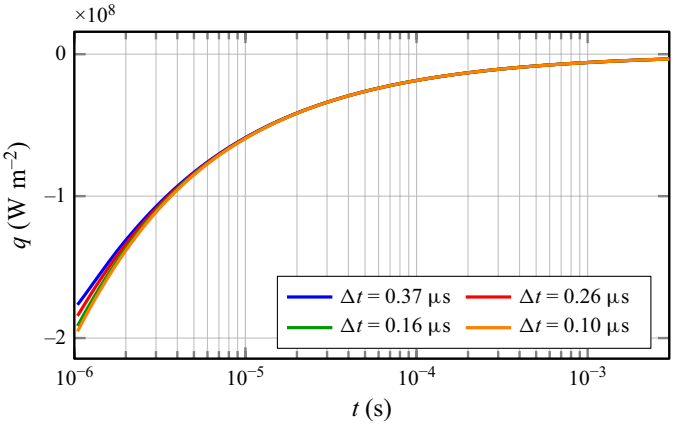


Figure 13. Surface heat flux $q(t)$ for a fixed through-thickness grid ($\Delta_z = 3.8\,\mu\text{m}$) at several time steps.

Appendix A. Grid and time independence study

The through-thickness mesh spacing and the time step used in the production runs are $\Delta z = 3.8\,\mu\text{m}$ and $\Delta t = 30.16\,\mu\text{s}$, respectively. Since temperature converges with relatively high time and grid spacings, grid convergence is assessed by comparing the interfacial heat flux $q(t)$ on successive refinements. We define the maximum relative error over the common time window I as

$$E_{\infty}^{(i)} = \max_{t \in I} \frac{|q_{i+1}(t) - q_i(t)|}{|q_{i+1}(t)|} \times 100\,\%, \tag{A1}$$

where i and $i+1$ denote successive refinement levels, with $i+1$ finer than i. We declare grid (and, analogously, time step) independence when $E_{\infty}^{(i)} \leqslant 2\,\%$. The corresponding grid- and time-independence plots are shown in figures 12 and 13.

Appendix B. Airflow past a rotating disc

For the sake of clarity, we report here the solution of the three-dimensional (3-D) boundary layer problem of air due to a rotating disc. For the derivation of the equations, the interested reader is referred to Kármán (1921) and Millsaps & Pohlhausen (1952).

https://doi.org/10.1017/jfm.2025.10978 Published online by Cambridge University Press

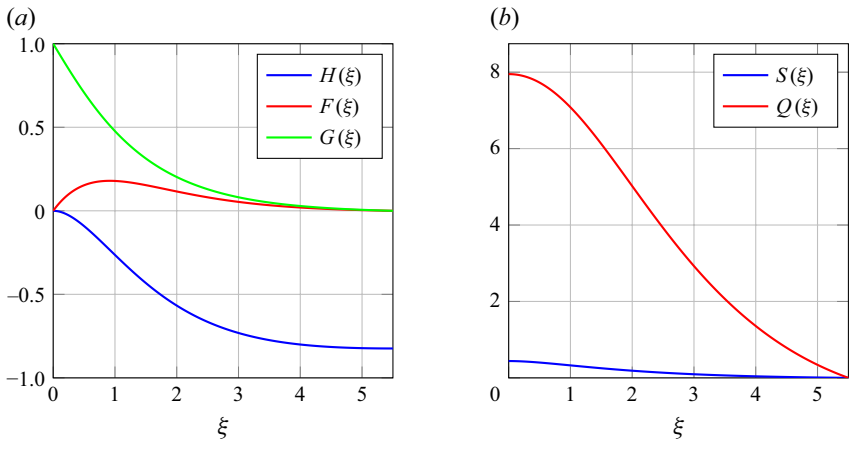


Figure 14. Solutions to the 3-D boundary-layer problem for a rotating disc. (*a*) Hydrodynamic components $H(\xi)$, $F(\xi)$ and $G(\xi)$. (*b*) Thermodynamic components $S(\xi)$ and $Q(\xi)$.

A dimensionless system of ODEs can be found by imposing

$$u_r = rf(z), \quad u_\theta = rg(z), \quad u_z = h(z), \quad p = p(z). \tag{B1}$$

For the thermal distribution,

$$t = r^2 s(z) + q(z) + t_\infty. \tag{B2}$$

The non-dimensional incompressible Navier–Stokes equations simplify to the following system:

$$F^2 - G^2 + HF' = F'', \tag{B3}$$

$$2FG + HG = G'', \tag{B4}$$

$$HH' + 2F' = P', \tag{B5}$$

$$2F + H' = 0; \tag{B6}$$

where

$$f = \omega F, \quad g = \omega G, \quad h = (\nu\omega)^{1/2} H, \quad p = \rho\nu\omega P, \quad z = \left(\frac{\nu}{\omega}\right)^{1/2} \xi; \tag{B7}$$

subject to the boundary conditions

$$F(0) = 0, \quad G(0) = 1, \quad H(0) = 0, \quad F(\infty) = 0, \quad G(\infty) = 0. \tag{B8}$$

The corresponding energy equation reduces to

$$Pr_a H S' - Pr_a H' S - Pr_a \left(F'^2 + G'^2\right) = S'', \tag{B9}$$

$$Pr_a H Q' - \left(4S + 12 Pr_a F^2\right) = Q''; \tag{B10}$$

subject to the following boundary conditions:

$$S'(0) = 0, \quad Q'(0) = 0, \quad S(\infty) = 0, \quad Q(\infty) = 0. \tag{B11}$$

Here, Pr_a represents the Prandtl number of air. The first set of four ODEs, given in (B3)–(B6), describes the hydrodynamic part of the problem, as proposed by Kármán (1921) and solved numerically by Cochran (1934). The solution to these equations is shown in figure 14(*a*), which presents the non-dimensional vertical, radial, and azimuthal velocity

https://doi.org/10.1017/jfm.2025.10978 Published online by Cambridge University Press

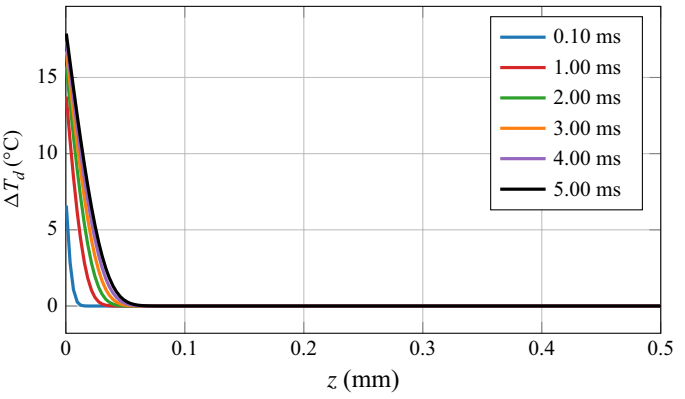


Figure 15. Temperature rise in the droplet, $\Delta T_d(z, t) = T_d - T_{d0}$, at selected times over z.

components $H(\xi)$, $F(\xi)$ and $G(\xi)$, respectively. The second set, (B9), (B10), governs the thermodynamic problem. The solution, displayed in figure 14(*b*), represents the non-dimensional temperature distribution $S(\xi)$ and $Q(\xi)$. The values of $S(0)$ and $Q(0)$ used in (2.6) are, respectively, 0.44 and 7.95.

Appendix C. Sensitivity to temperature-dependent properties

We assess the sensitivity of the analysis to temperature-dependent properties and, in particular, justify the constant-property approximation adopted in the main text. In the regime considered, interfacial heating is confined to a thin liquid layer adjacent to the wall ($\approx 50\,\mu$m; see figure 15), and variations of ρ, c_p and k are subdominant $\big(O(5\,\%)\big)$. The dominant temperature dependence enters through the viscosity, which affects the thermal problem only indirectly via the advective correction to the similarity velocity,

$$w(z, t) = -2\sqrt{\frac{\nu}{t}}\, g(\xi), \tag{C1}$$

with $\xi = z/\sqrt{\nu t}$. Thus, the influence of $\mu(T)$ is moderated both by the square-root dependence on ν and by the fact that, over the time window of interest, advection remains weaker than conduction.

To test this, we solve a 1-D coupled wall–liquid problem and compare a baseline case (properties evaluated at T_{d0}) with a conservative 'hot' case in which the liquid properties are evaluated at $T_{d0} + \Delta T_{d,max}$. The quantity $\Delta T_{d,max}$ is determined from a reference case similar to our experimental conditions, with the sapphire substrate at 30 °C and the droplet at 0 °C. Figure 15 shows the maximum temperature increase on the liquid side within the chosen time window, which is ≈ 18 °C. Comparing the wall-side temperature profiles for the hot-property and baseline cases shows that the difference $T_w^{hot} - T_w^{base}$ remains negligible over the examined times (figure 16). Even under this conservative comparison, these results support the use of temperature-independent properties at leading order for the conditions examined: the thermal perturbation is shallow and localised, conductive transport dominates over the advective correction, and viscosity-driven changes in the similarity velocity have a negligible effect on the predicted interfacial heat transfer.

Appendix D. Large-*Pr* validity check

We assess the large-*Pr* closure by comparing analytical (dashed) and numerical (solid) wall-side temperature profiles, plotted in the non-dimensional form

https://doi.org/10.1017/jfm.2025.10978 Published online by Cambridge University Press

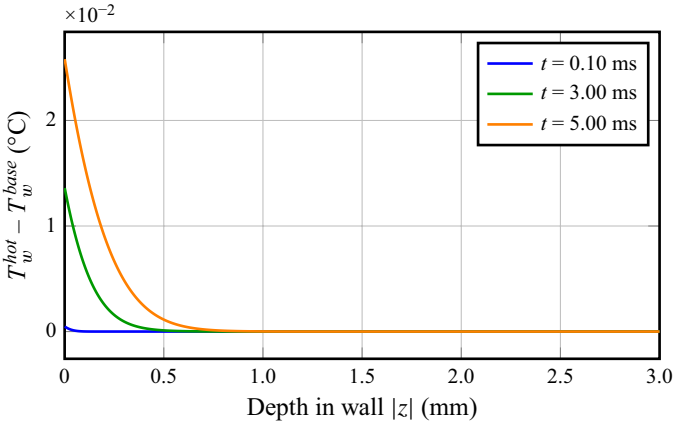


Figure 16. Wall-side temperature difference profiles.

$$\Theta = \frac{T - T_d}{T_w - T_d}, \tag{D1}$$

for three fluids spanning orders of magnitude in Pr: glycerol ($Pr \approx 1000$), water ($Pr \approx 7$) and mercury ($Pr \approx 0.01$). The corresponding wall-side non-dimensional temperature profiles Θ are shown in figure 17. For water and glycerol, the two curves agree closely over the window examined, supporting the use of the large-Pr closure; discrepancies increase for low-Pr mercury, as expected. We use a temperature difference between substrate and liquid of 30 °C to match the experiments, with $T_{d,0} = 20$ °C and $T_{w,0} = 50$ °C. This choice, rather than 0−30 °C, avoids invoking supercooling for glycerol.

Appendix E. Propagation of R_c uncertainty into h_{tc}

We quantify how the uncertainty of the fitted interfacial resistance R_c affects the modelled heat–transfer coefficient $h_{tc}(t) = q(t)/\Delta T$, where

$$\Delta T = T_{d0} - T_{w0}. \tag{E1}$$

Recall the closed–form expression used in the main text,

$$h_{tc}(t;\, R_c) = \frac{e_w e_d \sqrt{\pi}\, \theta'(0)}{\sqrt{t_R}\, \left(2e_w + e_d \sqrt{\pi}\, \theta'(0)\right)} \exp\left(\frac{t}{t_R}\right) \operatorname{erfc}\left(\sqrt{\frac{t}{t_R}}\right), \qquad t_R = (C R_c)^2, \tag{E2}$$

with

$$e_i = \sqrt{k_i\, \rho_i\, c_{p,i}}, \tag{E3}$$

$$C = \frac{e_d\, e_w}{e_d + e_w}, \tag{E4}$$

$$\theta'(0), \tag{E5}$$

as defined in the convection closure (see § 3).

For compactness, set

$$\beta = \sqrt{\pi}\, \theta'(0), \tag{E6}$$

$$H = \frac{e_w e_d\, \beta}{2e_w + e_d\, \beta}, \tag{E7}$$

https://doi.org/10.1017/jfm.2025.10978 Published online by Cambridge University Press

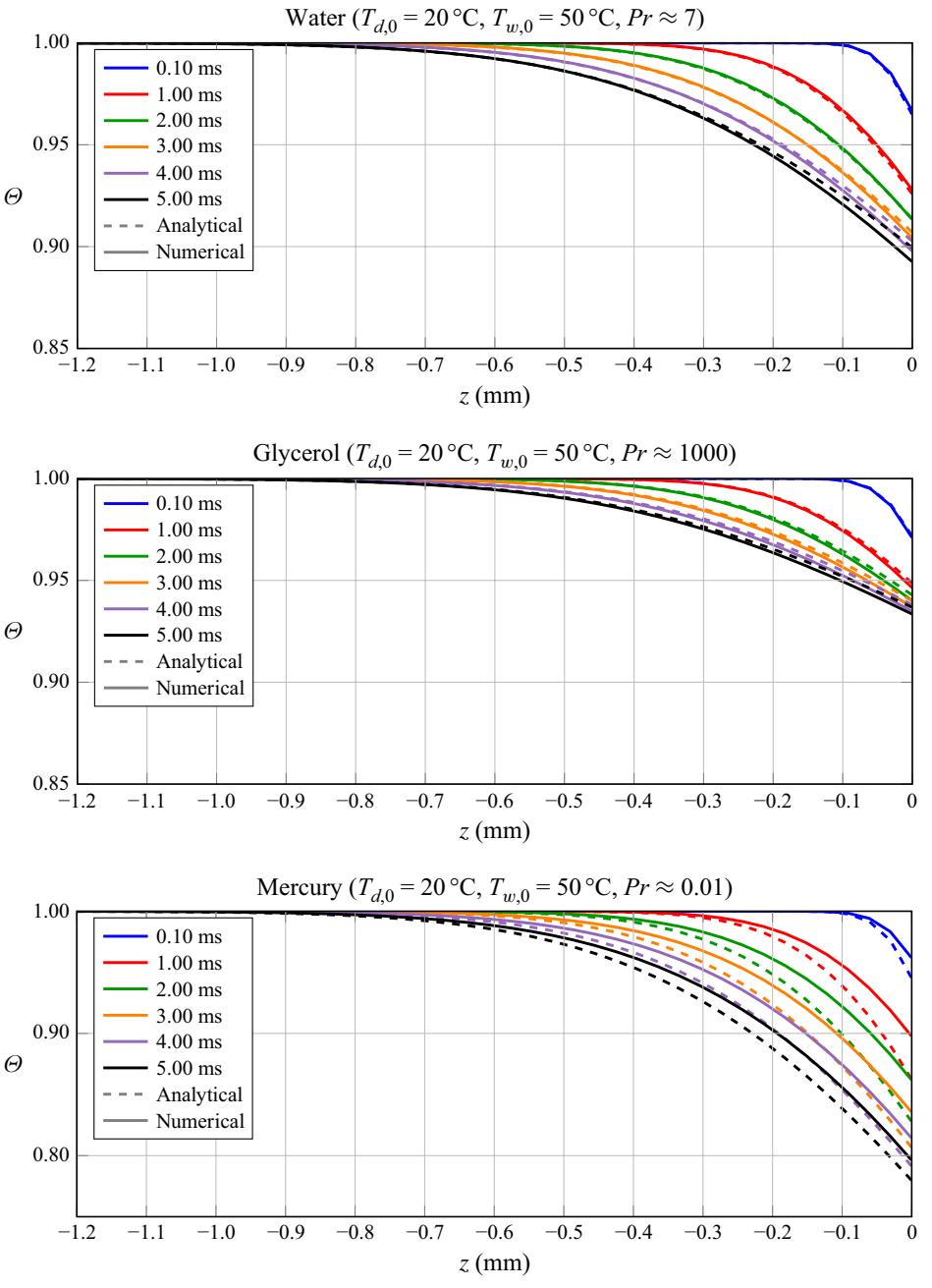


Figure 17. Wall-side non-dimensional temperature profiles Θ at six times (0.10–5.00 ms).

$$\chi = \frac{t}{t_R}, \tag{E8}$$

$$\Phi(\chi) = \exp(\chi)\,\mathrm{erfc}\left(\sqrt{\chi}\right), \tag{E9}$$

so that

$$h_{tc}(t;\, R_c) \;=\; H\, t_R^{-1/2}\, \Phi(\chi), \qquad t_R = (C R_c)^2. \tag{E10}$$

https://doi.org/10.1017/jfm.2025.10978 Published online by Cambridge University Press

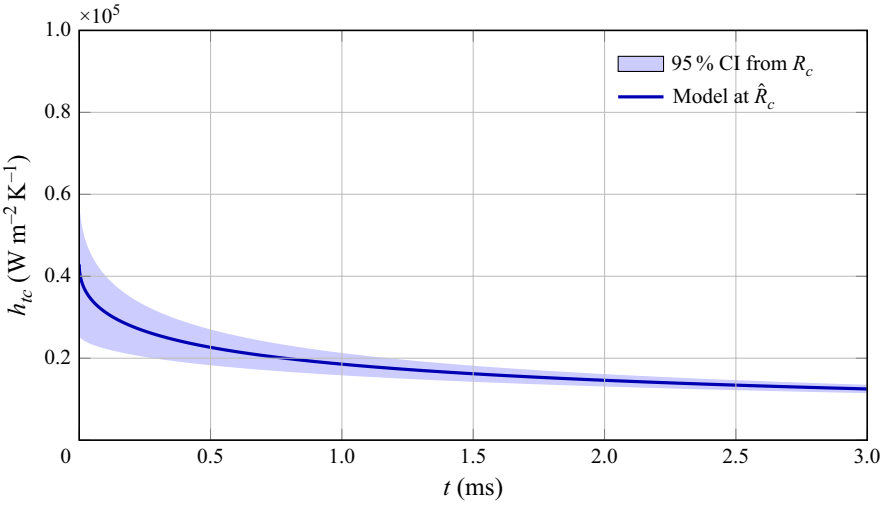


Figure 18. Propagation of R_c uncertainty into $h(t)$: best-fit curve $h(t;\,\hat{R}_c)$ with 95 % confidence band computed from (E13).

Let $\hat{R}_c$ be the point estimate and σ_{R_c} its standard error (e.g. from a 95 % CI $[R_c^{low},\,R_c^{high}]$ via

$$\sigma_{R_c} \approx \frac{R_c^{high} - R_c^{low}}{2 \times 1.96}\,). \tag{E11}$$

The analytic sensitivity of h_{tc} to R_c at $\hat{R}_c$ is

$$\frac{\partial h_{tc}}{\partial R_c}(t;\,\hat{R}_c) = \frac{H}{\hat{R}_c}\,t_R^{-1/2}\left[\frac{2}{\sqrt{\pi}}\sqrt{\chi} - (1+2\chi)\,\Phi(\chi)\right]_{R_c=\hat{R}_c}. \tag{E12}$$

A pointwise 95 % confidence band for h_{tc} due solely to the uncertainty in R_c is then

$$h_{tc}(t;\,\hat{R}_c) \pm 1.96\left|\frac{\partial h_{tc}}{\partial R_c}(t;\,\hat{R}_c)\right|\sigma_{R_c}. \tag{E13}$$

Figure 18 illustrates the confidence band from (E13).

References

Aboud, D.G.K. & Kietzig, A.-M. 2018 On the oblique impact dynamics of drops on superhydrophobic surfaces. Part I: sliding length and maximum spreading diameter. *Langmuir* **34**, 9879–9888.

Adam, C.D. 2012 Fundamental studies of bloodstain formation and characteristics. *Forensic Sci. Intl* **219** (1–3), 76–87.

Almohammadi, H. & Amirfazli, A. 2017 Understanding the drop impact on moving hydrophilic and hydrophobic surfaces. *Soft Matt.* **13** (10), 2040–2053.

Antonini, C., Amirfazli, A. & Marengo, M. 2012 Drop impact and wettability: from hydrophilic to superhydrophobic surfaces. *Phys. Fluids* **24** (10), 102104.

Antonini, C., Villa, F. & Marengo, M. 2014 Oblique impacts of water drops onto hydrophobic and superhydrophobic surfaces: outcomes, timing, and rebound maps. *Exp. Fluids* **55** (4), 1713.

Aziz, S.D. & Chandra, S. 2000 Impact, recoil and splashing of molten metal droplets. *Intl J. Heat Mass Transfer* **43** (16), 2841–2857.

Bartolo, D., Josserand, C. & Bonn, D. 2005 Retraction dynamics of aqueous drops upon impact on non-wetting surfaces. *J. Fluid Mech.* **545**, 329.

Bernardin, J.D., Stebbins, C.J. & Mudawar, I. 1997 Mapping of impact and heat transfer regimes of water drops impinging on a polished surface. *Intl J. Heat Mass Transfer* **40** (2), 247–267.

https://doi.org/10.1017/jfm.2025.10978 Published online by Cambridge University Press

BIRD, R.B., STEWART, W.E. & LIGHTFOOT, E.N. 1966 *Transport Phenomena*. John Wiley and Sons (WIE).
BREITENBACH, J., ROISMAN, I.V. & TROPEA, C. 2018 From drop impact physics to spray cooling models: a critical review. *Exp. Fluids* **59** (3), 55.
BRODBECK, S. 2012 Introduction to bloodstain pattern analysis. *J. Police Sci. Practice* **2**, 51–57.
BUKSH, S., ALMOHAMMADI, H., MARENGO, M. & AMIRFAZLI, A. 2019 Spreading of low-viscous liquids on a stationary and a moving surface. *Exp. Fluids* **60** (4), 557–574.
BUKSH, S., MARENGO, M. & AMIRFAZLI, A. 2020 Impacting of droplets on moving surface and inclined surfaces. *Atomiz. Sprays* **30** (8), 557–574.
CAO, Y., TAN, W. & WU, Z. 2018 Aircraft icing: an ongoing threat to aviation safety. *Aerosp. Sci. Technol.* **75**, 353–385.
CARDONE, G., ASTARITA, T. & CARLOMAGNO, G.M. 1994 IR heat transfer measurements on a rotating disk. In *Proceedings of the 1994 International Conference on Quantitative InfraRed Thermography*, QIRT Council.
CARSLAW, H.S. & JAEGER, J.C. 1959 *Conduction of Heat in Solids*, 2nd edn. Oxford University Press.
CHANDRA, S. & FAUCHAIS, P. 2009 Formation of solid splats during thermal spray deposition. *J. Therm. Spray Technol.* **18** (2), 148–180.
CHAZE, W., CABALLINA, O., CASTANET, G., PIERSON, J.-F., LEMOINE, F. & MAILLET, D. 2019 Heat flux reconstruction by inversion of experimental infrared temperature measurements – application to the impact of a droplet in the film boiling regime. *Intl J. Heat Mass Transfer* **128**, 469–478.
COCHRAN, W.G. 1934 The flow due to a rotating disc. *Math. Proc. Camb. Phil. Soc.* **30** (3), 365–375.
DHIMAN, R. & CHANDRA, S. 2005 Freezing-induced splashing during impact of molten metal droplets with high weber numbers. *Intl J. Heat Mass Transfer* **48** (25–26), 5625–5638.
ELFNER, M., SCHULZ, A., BAUER, H.-J. & LEHMANN, K. 2017 A novel test rig for assessing advanced rotor blade cooling concepts, measurement technique and first results. In *Volume 5A: Heat Transfer*. American Society of Mechanical Engineers.
EVANS, L.C. 2010 *Partial Differential Equations*, 2nd edn. Graduate Studies in Mathematics. American Mathematical Society.
FALSETTI, C., SISTI, M. & BEARD, P.F. 2021 Infrared thermography and calibration techniques for gas turbine applications: a review. *Infrared Phys. Technol.* **113**, 103754.
FAUCHAIS, P. 2004 Understanding plasma spraying. *J. Phys. D: Appl. Phys.* **37** (9), R86–R108.
GARCÍA-GEIJO, P., QUINTERO, E.S., RIBOUX, G. & GORDILLO, J.M. 2021 Spreading and splashing of drops impacting rough substrates. *J. Fluid Mech.* **917**, A50.
GARCÍA-GEIJO, P., RIBOUX, G. & GORDILLO, J.M. 2020 Inclined impact of drops. *J. Fluid Mech.* **897** (A12), A50.
GHOLIJANI, ALIREZA, FISCHER, SEBASTIAN, GAMBARYAN-ROISMAN, TATIANA & STEPHAN, PETER 2022 High resolution measurements of heat transfer during drop impingement onto a heated wall. In *Fluid Mechanics and Its Applications, Fluid Mechanics and Its Applications*, pp. 291–310. Springer International Publishing.
GHOLIJANI, A., SCHLAWITSCHEK, C., GAMBARYAN-ROISMAN, T. & STEPHAN, P. 2020 Heat transfer during drop impingement onto a hot wall: the influence of wall superheat, impact velocity, and drop diameter. *Intl J. Heat Mass Transfer* **153**, 119661.
GORDILLO, J.M., RIBOUX, G. & QUINTERO, E.S. 2019 A theory on the spreading of impacting droplets. *J. Fluid Mech.* **866**, 298–315.
JOSSERAND, C. & THORODDSEN, S.T. 2016 Drop impact on a solid surface. *Annu. Rev. Fluid Mech.* **48** (1), 365–391.
KAPITZA, P.L. 1941 The study of heat transfer in Helium II. *J. Phys. USSR* **4**, 181–210.
KÁRMÁN, T.V. 1921 Über laminare und turbulente Reibung. *Z. Angew. Math. Mech.* **1** (4), 233–252.
KEEGAN, M.H., NASH, D.H. & STACK, M.M. 2013 On erosion issues associated with the leading edge of wind turbine blades. *J. Phys. D: Appl. Phys.* **46** (38), 383001.
KOBAYASHI, R. 1994 Review: laminar-to-turbulent transition of three-dimensional boundary layers on rotating bodies. *J. Fluids Engng* **116** (2), 200–211.
LAAN, N., DE BRUIN, K.G., BARTOLO, D., JOSSERAND, C. & BONN, D. 2014 Maximum diameter of impacting liquid droplets. *Phys. Rev. Appl.* **4** (2), 044018.
LATKA, A., STRANDBURG-PESHKIN, A., DRISCOLL, M.M., STEVENS, C.S. & NAGEL, S.R. 2012 Creation of prompt and thin-sheet splashing by varying surface roughness or increasing air pressure. *Phys. Rev. Lett.* **109** (5), 054501.
LECLEAR, S., LECLEAR, J., ABHIJEET, PARK, K.-C. & CHOI, W. 2016 Drop impact on inclined superhydrophobic surfaces. *J. Colloid Interface Sci.* **461**, 114–121.

https://doi.org/10.1017/jfm.2025.10978 Published online by Cambridge University Press

MARENGO, M., ANTONINI, C., ROISMAN, I.V. & TROPEA, C. 2011 Drop collisions with simple and complex surfaces. *Curr. Opin. Colloid Interface Sci.* **16** (4), 292–302.

MARTINY, M., SCHIELE, R., GRITSCH, M., SCHULZ, A. & WITTIG, S. 1996 In situ calibration for quantitative infrared thermography. In *Proceedings of the 1996 International Conference on Quantitative InfraRed Thermography*, QIRT Council.

MILLSAPS, K. & POHLHAUSEN, K. 1952 Heat transfer by laminar flow from a rotating plate. *J. Aeronaut. Sci. (Inst. Aeronaut. Sci.)* **19** (2), 120–126.

MOHAMMAD KARIM, A. 2023 Physics of droplet impact on various substrates and its current advancements in interfacial science: a review. *J. Appl. Phys.* **133** (3), 030701.

MOREIRA, A.L.N., MOITA, A.S. & PANÃO, M.R. 2010 Advances and challenges in explaining fuel spray impingement: how much of single droplet impact research is useful? *Prog. Energy Combust. Sci.* **36** (5), 554–580.

MUNDO, C., SOMMERFELD, M. & TROPEA, C. 1995 Droplet-wall collisions: experimental studies of the deformation and breakup process. *Intl J. Multiphase Flow* **21** (2), 151–173.

NASTIC, A., PERSHIN, L. & MOSTAGHIMI, J. 2024 Microscale surface defects influence on thermally sprayed alumina droplets deformation and splashing dynamics. *ASME J. Heat Mass Transfer* **146** (5), 1–22.

OCHS, M., HORBACH, T., SCHULZ, A., KOCH, R. & BAUER, H.-J. 2009 A novel calibration method for an infrared thermography system applied to heat transfer experiments. *Meas. Sci. Technol.* **20** (7), 075103.

ORME, M. 1993 A novel technique of rapid solidification net- form materials synthesis. *J. Mater. Engng Performance* **2** (3), 399–405.

PIER, B. 2013 Transition near the edge of a rotating disk. *J. Fluid Mech.* **737**, R1.

POVAROV, O.A., NAZAROV, O.I., IGNAT'EVSKAYA, L.A. & NIKOL'SKII, A.I. 1976 Interaction of drops with boundary layer on rotating surface. *J. Engng Phys.* **31** (6), 1453–1456.

QUÉRÉ, D. 2008 Wetting and roughness. *Annu. Rev. Mater. Res.* **38** (1), 71–99.

QUETZERI-SANTIAGO, M.A., CASTREJÓN-PITA, A.A. & CASTREJÓN-PITA, J.R. 2019 The effect of surface roughness on the contact line and splashing dynamics of impacting droplets. *Sci. Rep.* **9** (1), 15030.

RANGE, K. & FEUILLEBOIS, F. 1998 Influence of surface roughness on liquid drop impact. *J. Colloid Interface Sci.* **203** (1), 16–30.

REGULAGADDA, K., BAKSHI, S. & DAS, S.K. 2018 Droplet ski-jumping on an inclined macro-textured superhydrophobic surface. *Appl. Phys. Lett.* **113** (10), 103702.

REIN, M. 2002 *Drop-Surface Interactions. CISM International Centre for Mechanical Sciences*. Springer.

RIBOUX, G. & GORDILLO, J.M. 2014 Experiments of drops impacting a smooth solid surface: a model of the critical impact speed for drop splashing. *Phys. Rev. Lett.* **113** (2), 024507.

RIBOUX, G. & GORDILLO, J.M. 2015 The diameters and velocities of the droplets ejected after splashing. *J. Fluid Mech.* **772**, 630–648.

ROISMAN, I.V. 2009 Inertia dominated drop collisions. II. An analytical solution of the Navier–Stokes equations for a spreading viscous film. *Phys. Fluids* **21** (5), 052104.

ROISMAN, I.V. 2010 Fast forced liquid film spreading on a substrate: flow, heat transfer and phase transition. *J. Fluid Mech.* **656**, 189–204.

ROISMAN, I.V., BERBEROVIĆ, E. & TROPEA, C. 2009 Inertia dominated drop collisions. I. On the universal flow in the lamella. *Phys. Fluids* **21** (5), 052103.

ROISMAN, I.V. & TROPEA, C. 2021 Wetting and icing of surfaces. *Curr. Opin. Colloid Interface Sci.* **53**, 101400.

SCHMIDT, J.B., BREITENBACH, J., ROISMAN, I.V. & TROPEA, C. 2020 Measurement of the heat flux during a drop impact onto a hot dry solid surface using infrared thermal imaging. In *Notes on Numerical Fluid Mechanics and Multidisciplinary Design*, pp. 553–562. Springer International Publishing.

SCHULZ, A. 2000 Infrared thermography as applied to film cooling of gas turbine components. *Meas. Sci. Technol.* **11** (7), 948–956.

SEKI, M., KAWAMURA, H. & SANOKAWA, K. 1978 Transient temperature profile of a hot wall due to an impinging liquid droplet. *J. Heat Transfer* **100** (1), 167–169.

SENDA, J., YAMADA, K., FUJIMOTO, H. & MIKI, H. 1988 The heat-transfer characteristics of a small droplet impinging upon a hot surface. *JSME Intl J. Heat Transfer Power Combust. Thermophys. Properties* **31** (1), 105–111.

SISTI, M., FALSETTI, C., BEARD, P. & CHANA, K. 2021 Infrared temperature measurements on high pressure turbine blades in the Oxford Turbine Research Facility: calibration and image processing techniques. In *14th European Conference on Turbomachinery Fluid Dynamics and Thermodynamics*. European Turbomachinery Society.

STEIRER, K.X., REESE, M.O., RUPERT, B.L., KOPIDAKIS, N., OLSON, D.C., COLLINS, R.T. & GINLEY, D.S. 2009 Ultrasonic spray deposition for production of organic solar cells. *Solar Energy Mater. Solar Cells* **93** (4), 447–453.

https://doi.org/10.1017/jfm.2025.10978 Published online by Cambridge University Press

STOW, C.D. & HADFIELD, M.G. 1981 An experimental investigation of fluid flow resulting from the impact of a water drop with an unyielding dry surface. *Proc. R. Soc. Lond.* **373** (1755), 419–441.

STUMPF, B., QEZELJEH, S.A., KAMAL, R., DEZITTER, F., MARTUFFO, A., ROISMAN, I.V. & HUSSONG, J. 2024 Drop impact onto a moving substrate: aerodynamic rebound. *Intl J. Multiphase Flow* **184**, 105113.

SWARTZ, E.T. & POHL, R.O. 1989 Thermal boundary resistance. *Rev. Mod. Phys.* **61** (3), 605–668.

TAROZZI, L., MUSCIO, A. & TARTARINI, P. 2007 Experimental tests of dropwise cooling on infrared-transparent media. *Exp. Therm. Fluid Sci.* **31** (8), 857–865.

TEODORI, E., PONTES, P., MOITA, A.S. & MOREIRA, A.L.N. 2018 Thermographic analysis of interfacial heat transfer mechanisms on droplet/wall interactions with high temporal and spatial resolution. *Exp. Therm. Fluid Sci.* **96**, 284–294.

THORODDSEN, S.T., ETOH, T.G. & TAKEHARA, K. 2008 High-speed imaging of drops and bubbles. *Annu. Rev. Fluid Mech.* **40** (1), 257–285.

VDI, E.V. 2013 *VDI-Wärmeatlas*. 11th edn. Springer.

WEISS, D.A. & YARIN, A.L. 1999 Single drop impact onto liquid films: neck distortion, jetting, tiny bubble entrainment, and crown formation. *J. Fluid Mech.* **385** (S002211209800411X), 229–254.

WORTHINGTON, A.M. 1877 XXVIII. On the forms assumed by drops of liquids falling vertically on a horizontal plate. *Proc. R. Soc. Lond.* **25** (171–178), 261–272.

XU, L. 2007 Liquid drop splashing on smooth, rough, and textured surfaces. *Phys. Rev. E Stat. Nonlinear Soft Matt. Phys.* **75** (5 Pt 2), 056316.

XU, L., ZHANG, W.W. & NAGEL, S.R. 2005 Drop splashing on a dry smooth surface. *Phys. Rev. Lett.* **94** (18), 184505.

YARIN, A.L. 2006 DROP IMPACT DYNAMICS: splashing, spreading, receding, bouncing. *Annu. Rev. Fluid Mech.* **38** (1), 159–192.

YARIN, A.L. & WEISS, D.A. 1995 Impact of drops on solid surfaces: self-similar capillary waves, and splashing as a new type of kinematic discontinuity. *J. Fluid Mech.* **283**, 141–173.

YEONG, Y.H., BURTON, J., LOTH, E. & BAYER, I.S. 2014 Drop impact and rebound dynamics on an inclined superhydrophobic surface. *Langmuir* **30** (40), 12027–12038.

ZHANG, Z., MA, L., LIU, Y., REN, J. & HU, H. 2021 An experimental study of rain erosion effects on a hydro-/ice-phobic coating pertinent to Unmanned-Arial-System (UAS) inflight icing mitigation. *Cold Reg. Sci. Technol.* **181**, 103196.

https://doi.org/10.1017/jfm.2025.10978 Published online by Cambridge University Press